fiTQun: A New Reconstruction Algorithm for Super-K

S. Berkman[1], P. de Perio[2], A. Konaka[3], A. Missert[4], H. Tanaka[1],
S. Tobayama[1], M. J. Wilking[3], E. D. Zimmerman[4]

[1]*University of British Columbia,* [2]*University of Toronto,* [3]*TRIUMF,*
[4]*University of Colorado*
E-mail: `wilking@triumf.ca`

July 3, 2013

Abstract

A new algorithm for reconstructing events at Super-K, called fiTQun, has been developed. In this note, the details of the algorithm are described and performance comparisons are made to previously existing algorithms.

Contents

1 Introduction

FiTQun is an event reconstruction algorithm for Super-Kamiokande. Each event at Super-K is a set of charges and times recorded for every photomultiplier tube (PMT) hit. Events can be further divided into time clusters of hits, called subevents, and for each subevent, there can be at most one charge and one time for each PMT. Hence, the determination of the kinematics of all particles in a subevent depends on making optimal use of, at most, $2 \times N_{PMTs}$ pieces of information.

Such problems naturally lend themselves to the use of likelihood functions, in which a probability density function (PDF) is constructed for each measurement: in this case, a PMT hit time or charge. The likelihood function is then a product of these PDFs, evaluated at the measured value. Since the PDFs vary as a function of the parameters that define the kinematics of the particles in each subevent, the likelihood is also a function of the particle parameters. The final reconstructed values of the track parameters are those that maximize the value of the likelihood function. This likelihood-based approach was also used by the MiniBooNE collaboration [1].

To determine the particular particle composition of a given subevent, many different reconstruction hypotheses can be tested. The number of particles that are above Cherenkov threshold in an event is determined by comparing a 1-ring hypothesis to a 2-ring hypothesis, a 2-ring hypothesis to a 3-ring hypothesis, etc., and deciding whether the improvement to the best fit likelihood that is gained by adding another ring is sufficient to indicate the presence of an additional particle. In a similar manner, particle identification is performed by comparing the best fit likelihoods of several different particle hypotheses (e.g. electron, muon, charged pion, etc.). Finally, in the particular case of separating neutral pions from electrons, a custom π^0 hypothesis fit is used to search for the additional ring from the π^0 decay.

For the summer 2013 T2K analysis, two versions of fiTQun were used: v3r0 and v3r1. The only change incorporated into fiTQun v3r1 was a correction for the average drift in the PMT gains as a function of time, which is only relevant for processing data events (more details can be found elsewhere [2]). Correspondingly, fiTQun v3r0 was run on the T2K and atmospheric Monte Carlo samples, and the hybrid pi0 data and Monte Carlo samples [4], while fiTQun v3r1 was run on the T2K and atmospheric data samples. This version of the technical note focuses on the features of fiTQun relevant to the summer 2013 analysis, namely the single ring electron and muon fits, and the π^0 fit. More information about the additional fiTQun features will be given in a future update.

2 The Likelihood Function

This section describes the construction of the likelihood function, which forms the basis of event reconstruction by fiTQun. The following discussion is for the simplest case of fitting a single ring event, i.e. an event with a single electron or a muon; however, the methods described below are straightforwardly generalized to more complicated multi-ring event topologies.

The kinematics of a single particle in the detector is characterized by the following seven parameters specifying its initial condition: vertex position $\boldsymbol{x}$, time t, zenith angle and azimuth of the direction θ, ϕ, and momentum p. Let $\mathbf{x}$ denote a set of such track parameters. For a given event, the most likely value for $\mathbf{x}$ is obtained by searching for the global maximum of the likelihood function, which is described below.

The inner detector (ID) of Super-Kamiokande consists of 11,129 PMTs. When a PMT detects

a Cherenkov photon, an electric signal is produced, and if the signal exceeds a discriminator threshold, the PMT registers a hit. The time of the hit as well as the integrated charge which was produced within the following ∼400ns time window are then recorded, which will be used for event reconstruction.

For a given event, fiTQun constructs a likelihood function based on the charge and time information from the ID PMTs, which is written as below:

$$L(\mathbf{x}) = \prod_j^{\text{unhit}} P_j(\text{unhit}|\mathbf{x}) \prod_i^{\text{hit}} \{1 - P_i(\text{unhit}|\mathbf{x})\} f_q(q_i|\mathbf{x}) f_t(t_i|\mathbf{x}) \tag{1}$$

The first index j runs over all PMTs which did not register a hit, and for each of the PMTs, the unhit probability $P_j(\text{unhit}|\mathbf{x})$ is multiplied, which is the probability of the j-th tube not registering a hit given track parameters $\mathbf{x}$. For the PMTs which did register a hit, the charge likelihood and the time likelihood as well as the hit probability is multiplied, where q_i and t_i represent charge and time observed by the i-th PMT respectively. The charge likelihood $f_q(q_i|\mathbf{x})$ is a probability density function of observing charge q_i at the i-th PMT given track parameters $\mathbf{x}$, and it is conditioned on a hit being produced. The time likelihood $f_t(t_i|\mathbf{x})$ is a probability density function for a hit being created at time t_i, given $\mathbf{x}$.

2.1 Predicted Charge

The dependence of each of the factors in the likelihood function on track parameters $\mathbf{x}$ can be simplified by introducing a quantity which is referred to as the predicted charge. The predicted charge μ_i for the i-th PMT, is the mean number of liberated photoelectrons at the PMT, given the track parameters $\mathbf{x}$. The likelihood function is then written as a function of μ_i as

$$L(\mathbf{x}) = \prod_j^{\text{unhit}} P_j(\text{unhit}|\mu_j) \prod_i^{\text{hit}} \{1 - P_i(\text{unhit}|\mu_i)\} f_q(q_i|\mu_i) f_t(t_i|\mathbf{x}), \tag{2}$$

where all the $\mathbf{x}$ dependence of the unhit probability and the charge likelihood is now confined in the predicted charges. $P_i(\text{unhit}|\mu_i)$ and $f_q(q_i|\mu_i)$ are, purely, properties of the PMTs and the electronics, independent of the Cherenkov photon emission process. The likelihood calculation is then performed in two steps; namely, calculation of the predicted charge for each PMT for a given set of track parameters, and evaluation of the likelihoods based on the predicted charges and the observed charge information. The time likelihood also makes use of the predicted charge, and the details are described in Section 2.6. Calculation of the predicted charge is done separately for direct light and indirect light, following the procedures described below.

2.2 Calculation of the Predicted Charge from Direct Light

The predicted charge from direct light is expressed as the following integral along the particle track

$$\mu^{\text{dir}} = \Phi(p) \int ds\, g(p, s, \cos\theta) \Omega(R) T(R) \epsilon(\eta), \tag{3}$$

where s is the distance the particle traveled along the track from its initial position. As in Figure 1, variables R, θ, η characterize the relative orientations of the particle and the PMT in question, and their values are uniquely defined as a function of s, once the initial condition of the particle is specified. Below is the description of each factor in the integrand in Eq.(3).
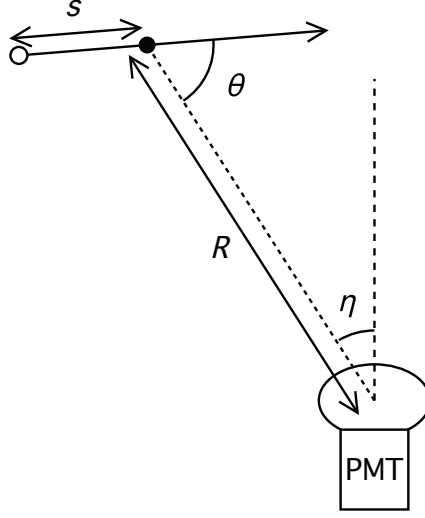
4

Figure 1: Schematic diagram describing the relevant variables for predicted charge calculation.

2.2.1 Charge Normalization Factor

The factor $\Phi(p)$ is a function of the particle's initial momentum, and it is proportional to the average total number of photons the particle at the specified initial momentum emits. $\Phi(p)$ also absorbs proportionality factors that are not accounted for by other factors in Eq.(3), such as the quantum efficiencies of the PMTs, and gives proper normalization to the predicted charge. For the quantum efficiencies, we apply corrections for PMT-by-PMT variations to $\Phi(p)$, based on the data obtained from detector calibrations. Finally, the overall normalization of $\Phi(p)$ is tuned using particle gun MC so that it gives unbiased reconstructed momentum.

2.2.2 Cherenkov Emission Profile

The factor $g(p, s, \cos\theta)$ is called the Cherenkov emission profile, and it represents the fraction of photons emitted per unit solid angle per unit track length at angle θ from the particle direction, when a particle with initial momentum p has traveled a distance s along the particle track. For each particle type, the profiles are generated at a range of discrete initial momentum values using a GEANT3-based detector simulation(SKDETSIM), and representative distributions for electrons and muons are shown in Figure 2.

It is seen from the figure that for electrons, photon emission peaks at $\cos\theta \approx 0.75$ regardless of the momentum, which corresponds to the opening angle of the Cherenkov cone from a particle with $\beta = 1$ in water. On the other hand, opening angle for muons are dependent on momentum, and we see the collapse of the Cherenkov cone as the particle travels. The showering nature of the electron Cherenkov rings manifests as the broad angular distribution of the profiles for electrons.

Since the total number of emitted photons are already accounted for by the factor $\Phi(p)$, we normalize $g(p, s, \cos\theta)$ such that
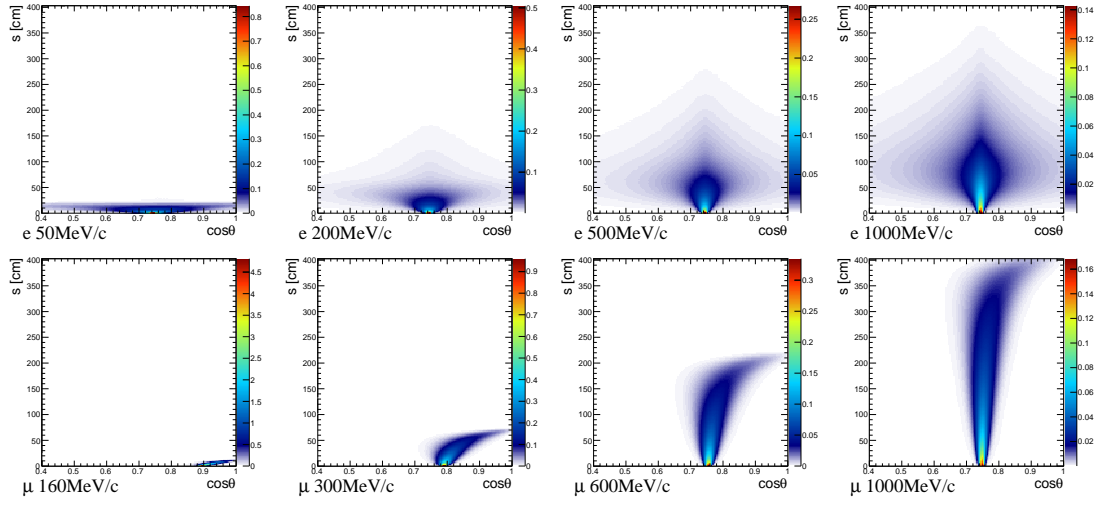
$$\int g(p, s, \cos\theta) ds d\Omega = 1. \tag{4}$$

5

Figure 2: Cherenkov emission profile $g(p, s, \cos\theta)$ for electrons(top) and muons(bottom) at a range of initial momentum. Horizontal axes represent the cosine of the angle from the particle direction, and vertical axes are the distance traveled from the initial position of the particle.

2.2.3 Solid Angle Factor

$\Omega(R)$ represents the solid angle subtended by a PMT at distance R, viewed from its normal. In order to reduce computation time, the factor is approximated by a function of a simple form:

$$\Omega(R) = \frac{a^2}{2(R^2 + a^2)}, \tag{5}$$

where $a = 25.4$cm is the radius of the PMT. The approximation holds sufficiently well at distance $R > 1$m.

2.2.4 Light Transmission Factor

The attenuation of direct light due to absorption and scattering in water is represented by the factor $T(R)$. This factor can be determined by using the following modified versions of SKDETSIM:

- **ScatToAbs (Direct Light Only):** All light that would have been scattered is instead immediately absorbed, so all light reaching the PMTs is direct light

- **NoScatNoAbs (Perfect Transmission):** No light is ever absorbed, scattered, or reflected, and all light that reaches the PMT glass produces a photoelectron (i.e. all PMT quantum efficiencies are set to unity).

Special Monte Carlo samples are generated in each of ScatToAbs and NoScatNoAbs modes. Each event consists of 100 simultaneous 3 MeV electrons that are started from a single vertex with an isotropic direction distribution. The goal of these "electron bombs" is to approximate a point source of Cherenkov light.

For the transmission function determination, electron bombs were generated along a line connecting PMT 8500 (middle of the top endcap) and PMT 10248 (middle of the bottom endcap)

6

in steps of 50 cm. The ratio of the number of photons that reach a PMT in ScatToAbs mode to that of NoScatNoAbs mode as a function of the distance to the PMT yields the transmission though the water. This distribution is then fit to an exponential function,

$$T(R) = \exp(-R/L^{\text{att}}), \tag{6}$$

where L^{att} is the attenuation length.

The results of the transmission function fits are shown in Figure 3. There is a clear discrepancy between the transmission measured by the top PMT and that measured by the bottom PMT. This is due to the known top/bottom asymmetry of the Super-K water quality. For now, the 72 m value measured at the top of the tank has arbitrarily been chosen for fiTQun.

More detailed studies have been performed to determine the transmission length as a function of depth (z-position). However, since the cause, size, and functional form of the top/bottom asymmetry is not yet well understood, we chose not to tune fiTQun to the existing top/bottom asymmetry model. In the future, the transmission function can be made to vary both as a function of both position and time.
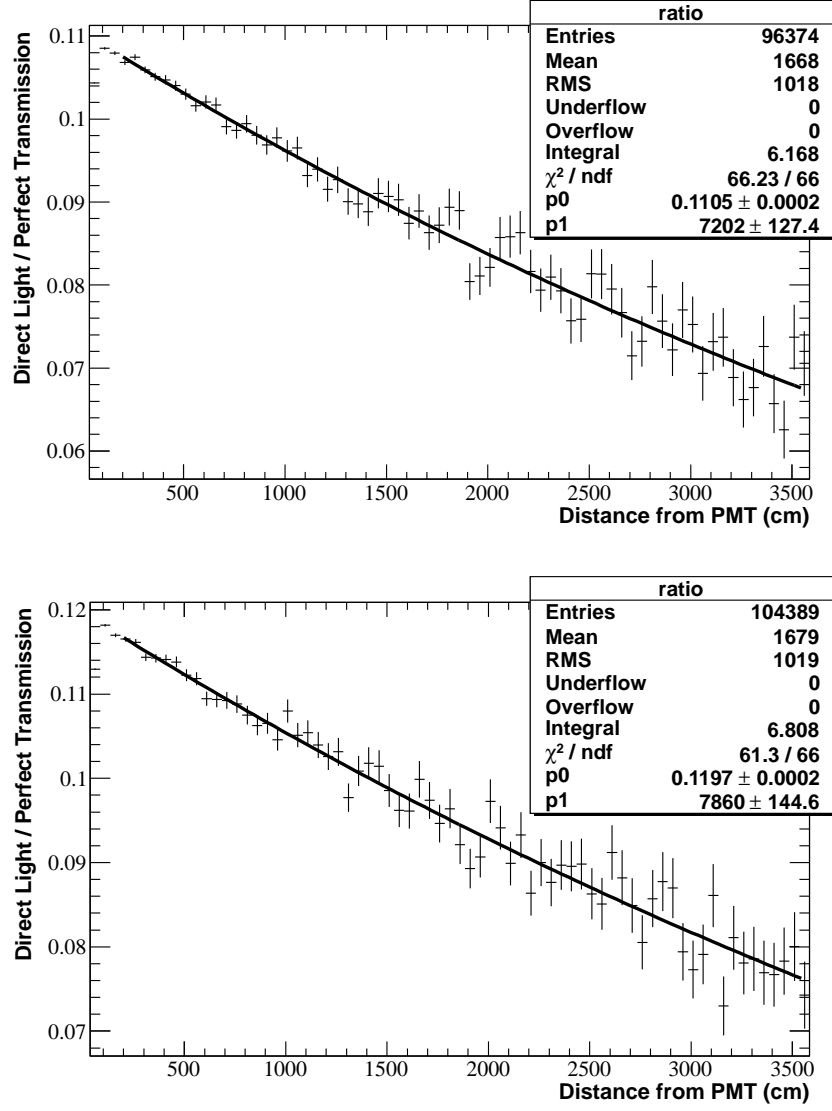
Figure 3: The transmission function fit for the PMT in the center of the top endcap is shown in the top figure, and the result for the PMT in the center of the bottom endcap is shown in the bottom figure. A longer transmission length is seen for the bottom PMT due to the known top/bottom asymmetry in the water quality at Super-K.

2.2.5 PMT Angular Acceptance

$\epsilon(\eta)$ is the PMT angular acceptance, which is a function of the angle η between the PMT normal and the direction of the particle position viewed from the PMT. The figure below is the acceptance curve obtained from the detector simulation, which also includes the effect of the shadowing by neighboring PMTs at high incident angle. The function is then fitted as indicated by the solid line in the figure, and the fit function is used in the fitter as $\epsilon(\eta)$. We adopt a normalization condition $\epsilon(0) = 1$, since $\Omega(R)$ was defined assuming $\eta = 0$.
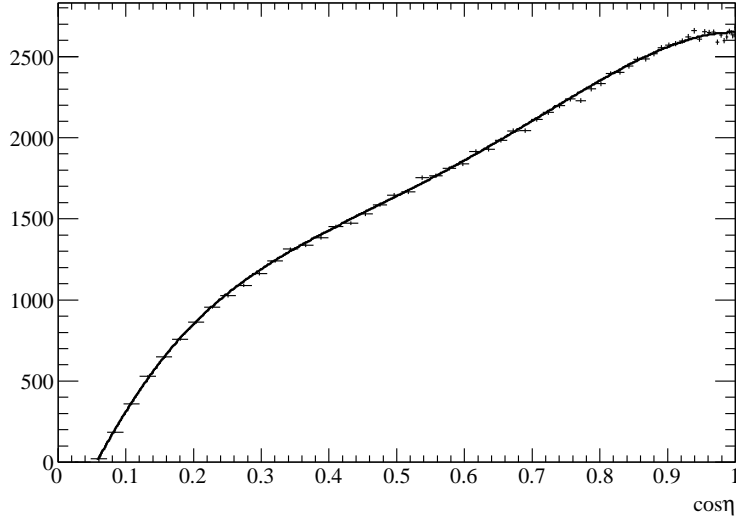

Figure 4: Angular acceptance of the PMTs, obtained from detector simulation, with a fitted curve overlaid as a solid line. Note that in the figure, the vertical axis in an arbitrary unit; in the fitter, the normalization is set so that the value of the function is 1 at $\eta = 0$.

2.3 Calculation of the Predicted Charge from Indirect Light

In addition to direct light which was considered above, indirect light must also be taken into account in order to properly predict the amount of charge deposited at each PMT. This includes light scattered in water as well as reflected light coming from detector components such as the black sheet and PMTs themselves. Similar to Eq.(3) for direct light, the predicted charge from indirect light is written as:

$$\mu^{\mathrm{sct}} = \Phi(p) \int ds \frac{1}{4\pi} \rho(p,s) \Omega(R) T(R) \epsilon(\eta) A(s), \tag{7}$$

where

$$\rho(p,s) \equiv \int g(p,s,\cos\theta) d\Omega \tag{8}$$

is the fraction of photons emitted per unit track length, at position s along the particle trajectory. When the factor $A(s)$ is removed from Eq.(7), the integrand represents the amount of direct light deposited from an imaginary isotropic light source whose location and the total light intensity

9

are the same as the charged particle described by the integrand of Eq.(3). In other words, in Eq.(7), photon emission described in Eq.(3) is averaged over all directions at each point on the particle track. The object

$$A(s) = A(x_{\mathrm{PMT}}, z_{\mathrm{vtx}}, R_{\mathrm{vtx}}, \varphi, \theta, \phi) \equiv \frac{d\mu^{\mathrm{sct}}}{d\mu^{\mathrm{iso,dir}}}, \tag{9}$$

which is referred to as the scattering table, is the ratio of the differential predicted charges deposited from point s along the track, by the indirect Cherenkov light from the charged particle in concern and the direct light from the imaginary isotropic source which was discussed above. Assuming that the Cherenkov opening angle does not change as a function of momentum, the momentum dependence is factored out from the scattering table by taking the ratio. The scattering table then depends only on the positional and directional alignment of the particle and the PMT, and a common table can be used for particles at any momentum. Note, again, that this is an approximation which assumes the Cherenkov opening angle to be independent of momentum and is fixed at the opening angle of particles at $\beta = 1$, when calculating the distribution of the indirect light.

Assuming the azimuthal symmetry of the detector, the scattering table is sufficiently expressed as a function of six variables which describe the orientations of the PMT and the particle in the detector, which are schematically shown in Figure 5. Note that the figure is for PMTs on the side wall, in which case the variable x_{PMT} in Eq.(9) corresponds to the PMT z position z_{PMT}. For PMTs on the top or the bottom wall, the PMT's distance from the vertical axis at the tank center R_{PMT} is used, instead of z_{PMT}.

In order to generate the scattering table, random 3MeV/c electron particle gun sample was generated using SKDETSIM with multiple scattering turned off, since such electrons can be considered as point Cherenkov sources with $\beta = 1$. Direct and indirect photons arriving at the PMTs are counted and filled separately into six-dimensional histograms, each axis corresponding to one of the six variables in Figure 5. Then, at each bin in the six-dimensional parameter space, the numerator $d\mu^{\mathrm{sct}}$ in Eq.(9) is obtained from the histogram for indirect photons, whereas the denominator $d\mu^{\mathrm{iso,dir}}$ is calculated by averaging the histogram for direct photons in terms of the particle direction. The scattering table is thus obtained as a six-dimensional histogram, and it is linearly interpolated in terms of the six variables at the time of evaluating the likelihood function.

2.4 Parabolic Approximation

As in Eqs.(3),(7), evaluation of the predicted charge involves an integral along the particle trajectory, which is computationally not feasible. We therefore introduce an approximation, which enables us to avoid the evaluation of the integral at the time of reconstructing an event.

Let $J(s)$ denote the last three factors in Eq.(3), which describes how the photons are received by the PMT:

$$J(s) \equiv \Omega(R)T(R)\epsilon(\eta) \approx j_0 + j_1 s + j_2 s^2. \tag{10}$$

This photon acceptance factor varies slowly as a function of s, and it is therefore reasonably approximated as a parabola, as in the figure below.

The coefficients j_n are obtained by evaluating $J(s)$ at three points on the particle trajectory, as indicated by hollow circles in the diagram. The evaluation is done at three points: the particle's initial position, the point at which 90% of Cherenkov light is emitted, and their midpoint.
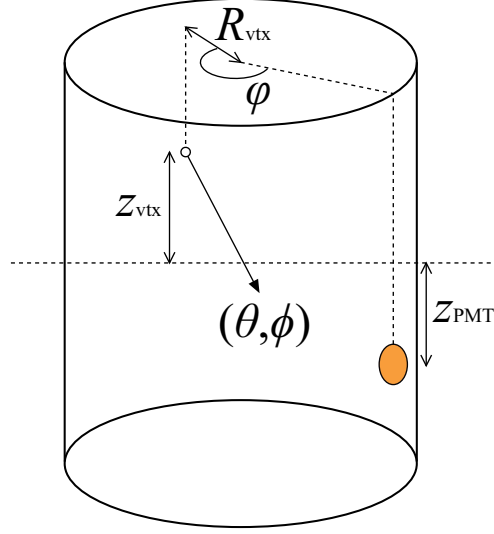
Figure 5: A schematic diagram which describes the relevant variables for the scattering table. For PMTs on the top or the bottom wall, the distance R_{PMT} of the PMT position from the vertical axis at the tank center is used, instead of z_{PMT}.
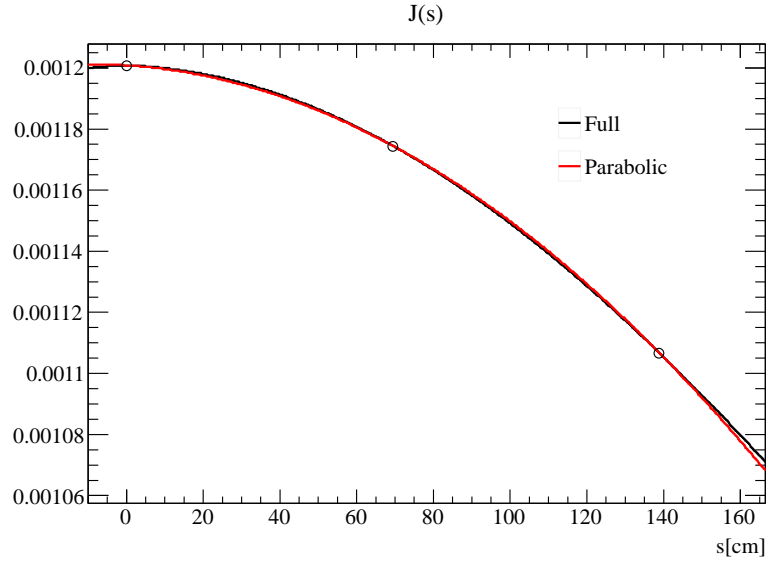

Figure 6: The photon acceptance factor $J(s)$ (black) overlaid with an approximating parabola (red). The coefficients for the parabola is obtained by evaluating $J(s)$ at the three points indicated by the hollow circles. The plot is for the initial conditions $R = 500\mathrm{cm}$, $\theta = 90°$, $\eta = 0°$.

Once the parabolic approximation of $J(s)$ is made, Eq.(3) reduces to

$$\mu^{\mathrm{dir}} = \Phi(p) \int ds g(s) J(s) \approx \Phi(p)(I_0 j_0 + I_1 j_1 + I_2 j_2), \tag{11}$$

where

$$I_n \equiv \int ds g(s) s^n. \tag{12}$$

The integral in Eq.(12) is done in advance, and I_n is obtained as a function of three parameters which specify the initial condition of the particle and its relative orientation to the PMT; namely, the initial values of the momentum p, the distance R from the particle to the PMT, and the angle θ between the particle direction and the line connecting the particle and the PMT positions. After performing the integral Eq.(12) at discrete bins in R, θ and p, I_n is fitted as a function of p at each R, θ bin, in order to smooth the likelihood surface. When reconstructing an event, I_n is linearly interpolated in terms of R and θ, after evaluation of the fit function at momentum p at the relevant R, θ bins is done.

For indirect light, since the scattering table $A(s)$ also tends to vary slowly as a function of s, we make the approximation $J(s)A(s) \approx k_0 + k_1 s + k_2 s^2$. The predicted charge calculation becomes:

$$\mu^{\mathrm{sct}} = \Phi(p) \int ds \frac{1}{4\pi} \rho(s) J(s) A(s) = \Phi(p) \frac{1}{4\pi}(k_0 + K_1 k_1 + K_2 k_2), \tag{13}$$

where

$$K_n \equiv \int ds \rho(s) s^n. \tag{14}$$

K_n is a function of p only, and it is therefore fitted as a function of p.

2.5 Unhit Probability and Charge Likelihood

Once the predicted charge for each PMT is calculated following the procedures described above, the unhit probabilities and the charge likelihoods in Eq.(2) is evaluated at the value of μ which is the sum of the predicted charges from direct and indirect light:

$$\mu = \mu^{\mathrm{dir}} + \mu^{\mathrm{sct}}. \tag{15}$$

Since the predicted charge μ is the mean number of photoelectrons liberated at a PMT, the actual number of photoelectrons should obey a Poisson distribution with mean μ. Therefore, the probability of no photoelectron being produced is $e^{-\mu}$. However, in order to take into account the PMT threshold effect, a correction up to the third order is applied in the expression of the unhit probability:

$$P(\mathrm{unhit}|\mu) \approx (1 + a_1 \mu + a_2 \mu^2 + a_3 \mu^3) e^{-\mu}. \tag{16}$$

The coefficients a_n were obtained from the detector simulation, and the figure below shows the unhit probability with and without the correction applied, compared with the true values obtained from the simulation.

The charge likelihood $f_q(q|\mu)$ was obtained by generating photoelectrons following Poisson statistics with mean μ directly at the PMTs in the detector simulation, and taking the distribution of the measured charge for the hit PMTs. The figure below shows the obtained normalized charge likelihood distribution at a range of predicted charge values. In order to smooth the likelihood surface, the normalized charge distributions are then fitted by a polynomial as a function of μ at each fixed value of q. When evaluating the likelihood for a given event, the fit parameters
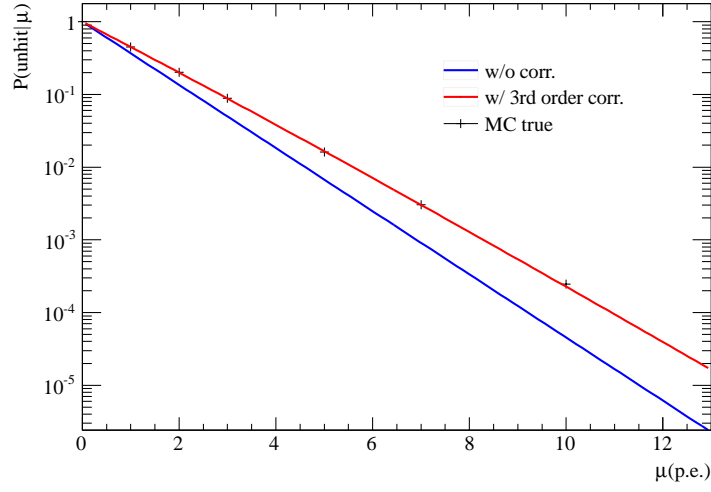
Figure 7: The unhit probability $P(\text{unhit}|\mu)$ with(red) and without(blue) the correction of the PMT threshold effect. The data points show the values obtained from detector simulation.
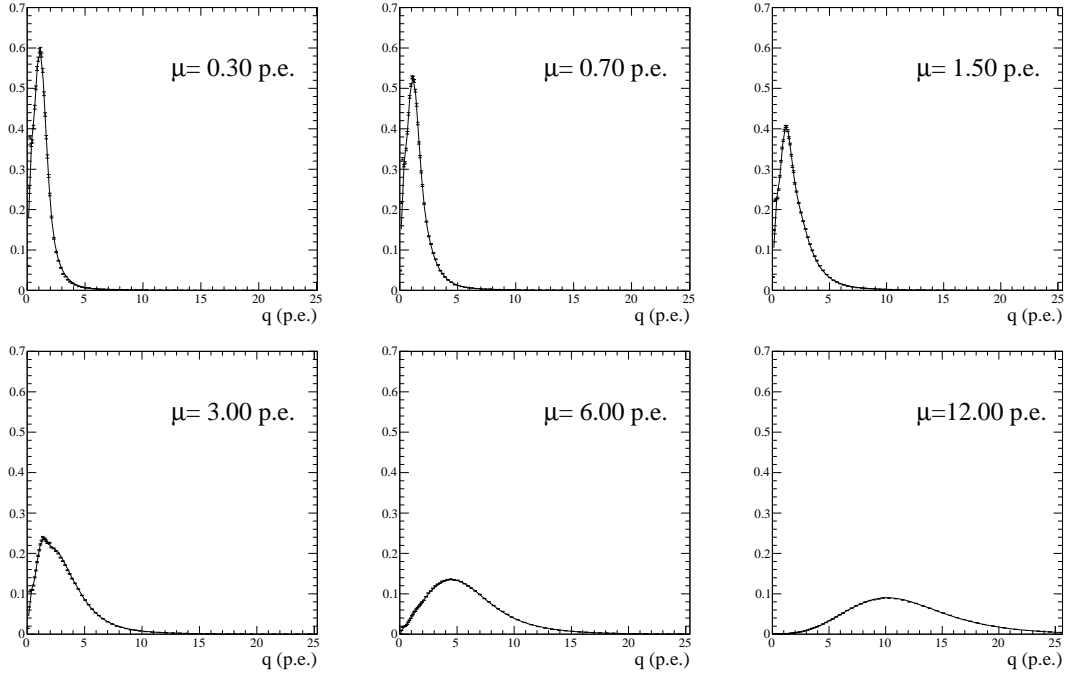

Figure 8: The normalized charge likelihood $f_q(q|\mu)$ at a range of predicted charge μ. The data points are obtained from the detector simulation, and the solid lines indicate the fitted function, which is used when evaluating the likelihood in the fitter.

263 are linearly interpolated in terms of the observed charge q, and the resulting polynomial function
264 is evaluated at μ.

265 Through detector calibrations, it is known that the PMT gain changes over time, which
266 results in charge scale variation. The overall detector-wide variation of the charge scale has been
267 monitored and measured by the peak position of the 1p.e. distribution, and its data during the
268 SK4 period is readily available. In order to compensate for this effect at the reconstruction level,
269 when applying fiTQun on data events, the measured charge q for all hit PMTs are scaled prior
270 to evaluating the charge likelihood by a single detector-wide correction factor, which is obtained
271 run-by-run from the 1p.e. peak data mentioned above. For more details, refer to [2].

2.6   Time Likelihood

273 The time likelihood $f_t(t_i|\mathbf{x})$ in Eq.(1) depends on the particle track parameters $\mathbf{x}$ as well as the
274 PMT position *etc.* in a complex way. Since it is impractical trying to accurately account for all
275 such dependencies, we approximate the time likelihood, starting by expressing the likelihood in
276 terms of the residual hit time t_i^{res} which is defined as below, instead of the raw hit time t_i:

$$t_i^{\mathrm{res}} \equiv t_i - t - s_{\mathrm{mid}}/c - |\boldsymbol{R}_{\mathrm{PMT}}^i - \boldsymbol{x} - s_{\mathrm{mid}}\boldsymbol{d}|/c_n. \tag{17}$$

277 $\boldsymbol{x}, t$ are vertex position and time, $\boldsymbol{d}$ is the particle direction, s_{mid} represents half the track length,
278 $\boldsymbol{R}_{\mathrm{PMT}}^i$ is the position of the i-th PMT, and c_n is the speed of optical photons in the water. t_i^{res}
279 therefore subtracts the expected direct photon arrival time from the hit time, assuming the
280 Cherenkov photons are emitted at the track midpoint. We then make an approximation that
281 the time likelihood depends only on t_i^{res}, the predicted charge from direct light μ^{dir}, that from
282 indirect light μ^{sct}, and the particle's momentum p. Since a hit is produced by the first photon
283 arriving at a PMT, the width of the residual time distribution decreases as photon statistics
284 increases, and such effect is characterized well by the predicted charge. We consider direct
285 light and indirect light separately, since they have distinct residual hit time distributions. The
286 momentum translates to the width of the residual time distribution, since the photon time-
287 of-flight correction in Eq.(17) becomes less accurate as the particle track becomes longer, and
288 the distribution becomes wider. All other dependence on the particle-PMT configurations is
289 averaged out in this approximation, and the information is embedded in the predicted charge.
290 We then further assume that all indirect photons arrive after the direct photons; i.e., an indirect
291 photon causes a hit only if there were no direct photons observed at a PMT. The time likelihood
292 can then be written as:

$$f_t(t_i^{\mathrm{res}}) = w f_t^{\mathrm{dir}}(t_i^{\mathrm{res}}) + (1 - w) f_t^{\mathrm{sct}}(t_i^{\mathrm{res}}), \tag{18}$$

293 where

$$w \equiv \frac{1 - e^{-\mu^{\mathrm{dir}}}}{1 - e^{-\mu^{\mathrm{dir}}} e^{-\mu^{\mathrm{sct}}}}, \tag{19}$$

294 and $f_t^{\mathrm{dir}}(t_i^{\mathrm{res}})$, $f_t^{\mathrm{sct}}(t_i^{\mathrm{res}})$ are normalized residual time PDFs for direct light and indirect light
295 respectively, at the given predicted charge and momentum values. We thus construct the time
296 likelihood on-the-fly by combining the time PDFs for direct and indirect light based on their
297 predicted charge values.

2.6.1 Direct Light Time PDF

The residual time PDF for direct light $f_t^{\mathrm{dir}}(t^{\mathrm{res}})$ is assumed to be a Gaussian, with its peak position and σ being dependent on μ^{dir} and momentum p. In order to produce the residual time distribution, particle gun MC samples are generated at various fixed momentum values, and for each momentum a t^{res}-$\log \mu^{\mathrm{dir}}$ 2-d histogram is filled. The t^{res} distribution is then fitted by a Gaussian at each $\log \mu^{\mathrm{dir}}$ bin, and its mean and the σ are fitted by a sixth-order polynomial in $\log \mu^{\mathrm{dir}}$. Finally, each of the polynomial fit parameters is fitted as a function of momentum. Thus, we have parameterized the direct light residual time PDF $f_t^{\mathrm{dir}}(t^{\mathrm{res}})$ as a smooth function of μ^{dir} and p, and the resulting PDF, as well as the original distribution obtained from the MC, are shown for electrons and muons in Figure 9 and 10.
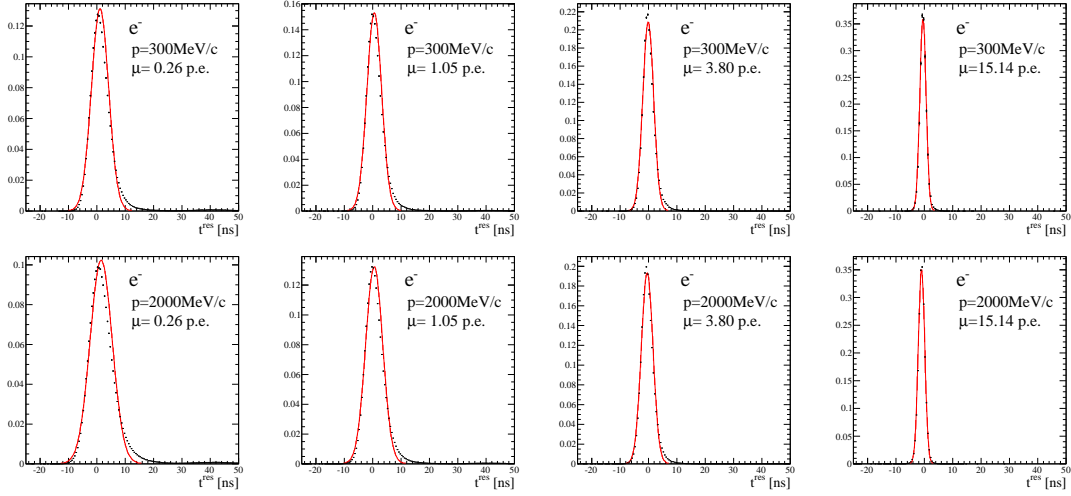

Figure 9: The direct light residual time PDF $f_t^{\mathrm{dir}}(t^{\mathrm{res}})$ for electrons, at a range of predicted charge μ^{dir}. The top row is for $p = 300\mathrm{MeV/c}$, and the bottom is for $p = 2000\mathrm{MeV/c}$. The data points indicate the original distributions obtained from the MC simulation, and the red curves are the Gaussian PDFs which we have parameterized as a function of μ^{dir} and p.

2.6.2 Indirect Light Time PDF

The residual time PDF for indirect light is currently modeled in fiTQun as:

$$f_t^{\mathrm{sct}}(t^{\mathrm{res}}) = 1 \Big/ \left(\sqrt{\frac{\pi}{2}} \sigma + 2\gamma \right) \times \begin{cases} \exp(-\tau^2/2\sigma^2) & (\tau < 0) \\ (\tau/\gamma + 1)\exp(-\tau/\gamma) & (\tau > 0) \end{cases} , \tag{20}$$

where $\tau = t^{\mathrm{res}} - 25\mathrm{ns}$, $\sigma = 8\mathrm{ns}$ and $\gamma = 25\mathrm{ns}$. The functional form was determined so that it reproduces a typical shape of the indirect light residual time distribution, and it has a characteristic long right side tail due to reflected light. No μ^{sct} or momentum dependence is considered at the present moment.
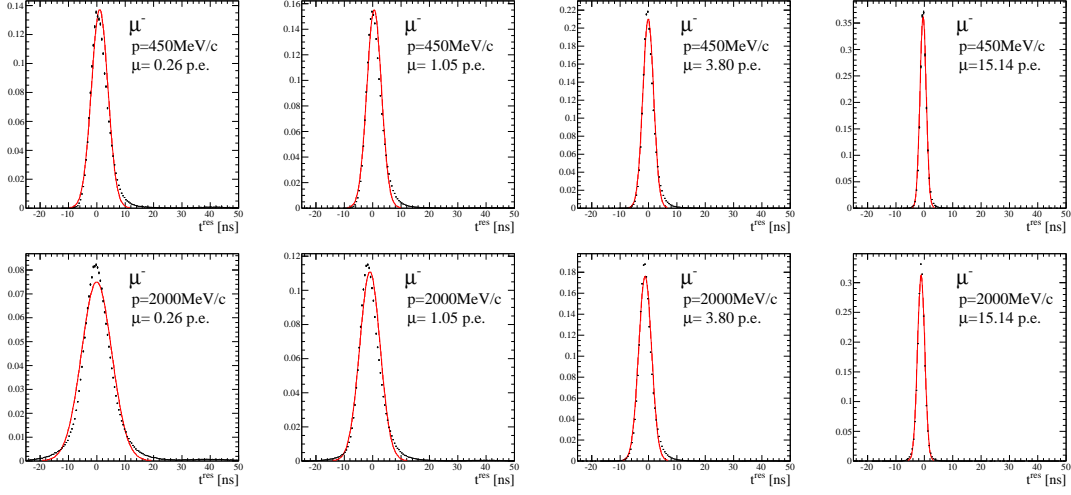
Figure 10: The direct light residual time PDF $f_t^{\mathrm{dir}}(t^{\mathrm{res}})$ for muons, at a range of predicted charge μ^{dir}. The top row is for $p = 450\mathrm{MeV/c}$, and the bottom is for $p = 2000\mathrm{MeV/c}$. The data points indicate the original distributions obtained from the MC simulation, and the red curves are the Gaussian PDFs which we have parameterized as a function of μ^{dir} and p.

3 The Vertex Pre-fitter

As it was mentioned earlier, event reconstruction in fiTQun is done by searching for the global maximum of the likelihood function. In practice, that is done by minimizing the negative log likelihood($-\ln L$) by varying all the fit parameters simultaneously using MINUIT. Despite the efforts that were made to make the likelihood surface smooth, local minima of $-\ln L$ inevitably exist. Therefore, it is important to seed the fit parameters with values which are reasonably close to the global minimum, in order to prevent the fit from converging at such local minima.

The vertex pre-fitter is a fast algorithm which uses only the hit time information from the PMTs to estimate the vertex position and time, and it is run at the beginning of processing every event. The estimation is done by searching for the vertex position $\boldsymbol{x}$ and time t, which maximizes the vertex goodness which is defined as:

$$G(\boldsymbol{x}, t) \equiv \sum_i^{\mathrm{hit}} \exp(-(T_{\mathrm{res}}^i/\sigma)^2/2), \tag{21}$$

where

$$T_{\mathrm{res}}^i \equiv t_i - t - |\boldsymbol{R}_{\mathrm{PMT}}^i - \boldsymbol{x}|/c_n. \tag{22}$$

T_{res}^i is the residual hit time, which is similar to Eq.(17); however, a point light source located at the vertex is assumed in this case. When the vertex position and time get close to their true values, T_{res}^i distribute near zero, which results in a large value of the goodness. The pre-fitter first maximizes the goodness by performing an iterative coarse grid-search in space and time, gradually shrinking the grid size and σ. After the grid search is done, a MINUIT minimization of $-G(\boldsymbol{x}, t)$ is performed with $\sigma = 4\mathrm{ns}$, which provides the final seed values for vertex and time.

16

4 Subevent Algorithms

This section describes how fiTQun treats subevents, i.e., particle activities in the detector that are separated in time. An event at Super-K is defined as PMT activities that happen near an event trigger in time, and some events have multiple subevents. A typical example is a muon decaying into an electron, in which case the primary muon and the decay electron register as separate subevents. The methods described below searches for such subevents, which enables us to count the number of decay electrons that are associated with an event.

4.1 The Peak Finder

As stated in the previous section, the vertex goodness Eq.(21) takes a large value when it is evaluated at the vertex position $\boldsymbol{x}$ and time t which are close to where an actual particle is located, since in such a case the residual hit time distributes near zero for hits that are produced by direct light emitted by the particle. Using this fact, the peak finder searches for subevents by fixing the vertex position $\boldsymbol{x}$ at the value the vertex pre-fitter returned, and scanning the goodness while varying the time t. Assuming that the vertex positions of both the primary particles and the decay electrons lie close to the pre-fit vertex, subevents appear as large peaks in the distribution of the goodness as a function of t.

After the vertex pre-fit is performed, the peak finder scans the goodness every 8ns step, starting at ∼300ns before the event trigger. The parameter σ in Eq.(21) is set to 6.3ns, which was optimized for the step size. Figure 11 is an example of the distribution of the goodness for an event with a single muon and a decay electron, where the dashed lines indicate true particle time and black dots show the scan points.
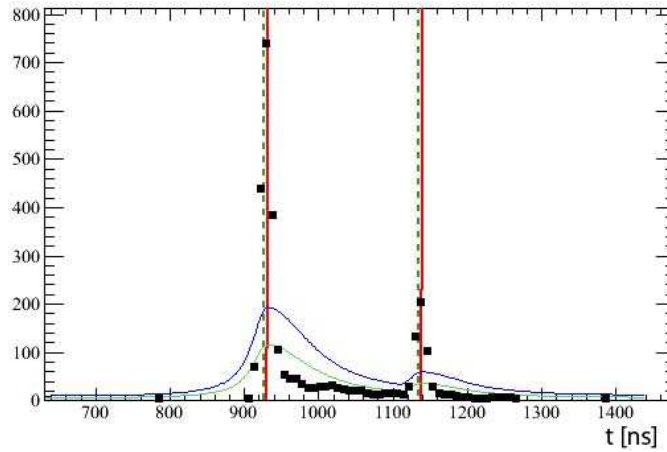

Figure 11: Distribution of the scanned goodness $G(\boldsymbol{x}, t)$ as a function of time t, for an example event with a muon primary and a decay electron. The vertical dashed lines indicate true particle time, the black dots are the goodness scan points, and the blue and green curves represent threshold curves which are used for subevent peak selection. The red vertical lines indicate the time of the subevent peaks which are found in this event.

In order to select subevent peaks in this distribution, we define a threshold curve $F(t)$ which

17

is expressed as:

$$F(t) \equiv 0.25 \max_{i \in M} \{ G(\boldsymbol{x}, t_i) f(t - t_i) \} + \eta, \tag{23}$$

where

$$f(\tau) \equiv \frac{1}{1 + (\tau/\gamma)^2}, \quad \gamma = \begin{cases} 25\text{ns} & (\tau < 0) \\ 70\text{ns} & (\tau > 0). \end{cases} \tag{24}$$

M represents all local maxima of goodness scan points, i.e. a scan point which is higher than the neighboring two, that has a goodness value larger than a constant threshold $\eta = 9$, which is described in more detail below. The blue curve in the figure represents $F(t)$, and the green curve is $0.6F(t)$. A subevent peak is defined as the first local maximum scan point which lies above the blue curve. The scan then continues onto later time searching for another peak, and a local maximum is ignored even if it was above the blue curve, if there is no scan point after the previous found peak went below the green curve. We employ this double-threshold criterion in order to reduce fake peaks, which follows a real subevent peak often in case the vertex estimation was poor.
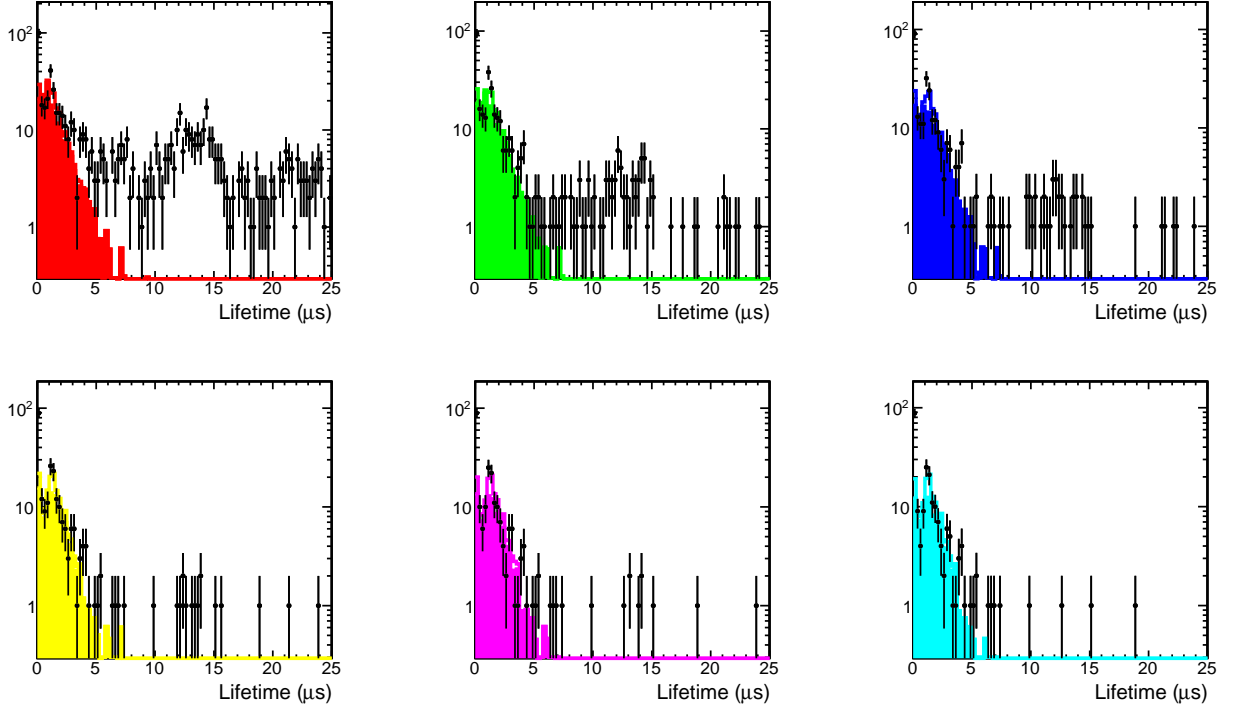

Figure 12: Δt ("Lifetime") between the 1st and 2nd peaks, where the 2nd peak was not matched to a Muechk peak for data (points) and MC (histogram). The panels from left to right, starting from the top row, correspond to $\eta = 7$ (red), 9 (green), 11 (blue), 13 (yellow), 15 (magenta) and 17 (cyan). The filled histograms correspond to events that were matched to within 50 ns of the birth of a true particle.

The constant threshold $\eta = 9$ was tuned using the atmospheric neutrino sample to minimize the false peak rate while maintaining good data and MC agreement of the overall performance of the peak finder. It was known that the existing APfit algorithm, Muechk, has a relatively
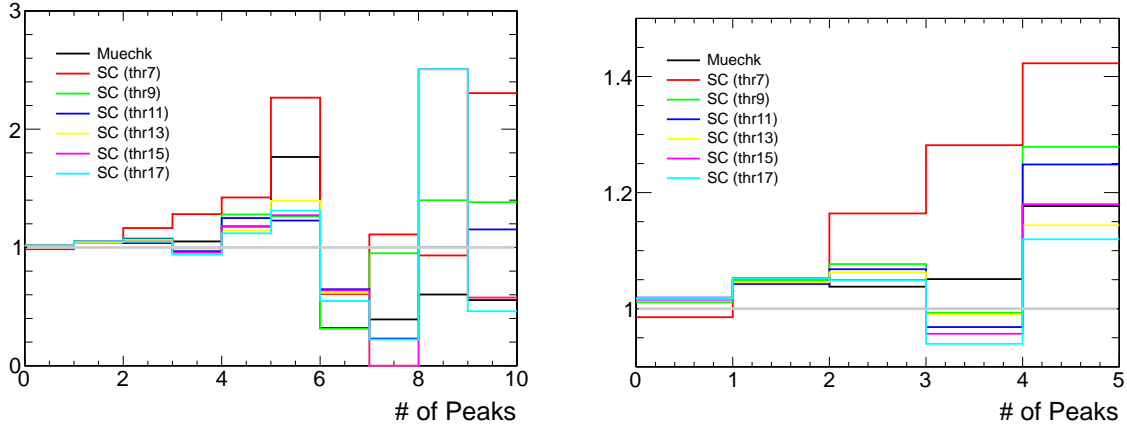
18

Figure 13: Data/MC ratio of the number of peaks in the atmospheric neutrino sample. "SC" refers to the peak finder and "thr" corresponds to η. The right panel is a zoom of the left panel.

low false peak rate. Hence, Muechk is used as a reference in Figure 12 where only peaks that are found by the peak finder which were not found by Muechk are plotted. A clear population of events around $10 < \Delta t < 15\mu$s can be seen, corresponding to the typical time for PMT afterpulsing. These false peaks are removed with increasing η. Note some small number of events near $\Delta t = 2\mu$s, which corresponds to the typical PMT recovery time that can produce a spike in the hit-time distribution after a significant PMT dead-time. The selection of $\eta = 9$ was also motivated by good data/MC agreement and a similar efficiency to Muechk[1]. This can be seen in Figure 13 which shows the data/MC ratio of the number of peaks for Muechk and various values of η.

The number and the time of the peaks that are found by this method are reported as the number and the time of the subevents associated with the event.

4.2   The spliTChan Hit Clustering Algorithm

This section describes the spliTChan algorithm, used for grouping together hits that are neighboring in time which most likely come from particle activity in the detector. A group of hits is referred to as a "time cluster". This would be a simple problem if the PMTs and electronics were noiseless such that any hits that are produced would be from Cerenkov light only. However, this is not the case, and special care must be taken when constructing time clusters.

The algorithm follows the high energy (HE) software trigger (SWT) previously referred to as the "event trigger", which is in principle another time cluster-finding algorithm. The SWT scans the raw time information and looks for some time window where the number of hits is above some threshold. It then extracts a time window containing these hits and returns it as an event. Ideally, one should only need a single stage for hit clustering, however the SWT is implemented at a lower level in the analysis and we could not easily modify it due to time constraints. Hence, spliTChan is applied to the event that is returned by the SWT.

The HE SWT typically places the start of the rise in the number of hits at t~1000 ns, so spliTChan uses hits at t > 800 ns to account for uncertainties on the position of the rise and

---

[1]The efficiency for decay-e detection efficiency was checked with stopping cosmic muon data and MC, and is similar to Muechk.

since the event is delivered including information much earlier than the HE trigger. The SWT also provides an "out-of-gate" flag for each hit, which is somewhat redundant with the minimum time requirement, and other issues that render a hit unusable for the event. spliTChan ignores these out-of-gate hits. To determine the final set of hits to use, a charge threshold of 0.3 pe is applied.

The procedure to build a time cluster is a follows:

1. Bin the raw hit-time distribution into 10 ns bins.

2. Find the time, t_{start}, where a 70 ns window has $nHits_{70} > 9$ hits. This threshold was determined from noise-only MC. Shift t_{start} to 30 ns earlier ($t_{start} = t_{start} - 30$ ns) to catch any early hits.

3. Scan through time until the 70 ns time window has $nHits_{70} \leq 9$ hits and the time difference between t_{start} and the end of the current time window, t_{end}, is ≥ 70 ns.

4. Extend the end time by $t_{end} = t_{end} + t_{extend}$, where $t_{extend} = max(0, -\frac{320}{800} \times nHits + 320)$ and $nHits$ is the total number of hits in the cluster prior to extension. This is designed to catch late hits from, for example, reflected light. The extension is larger for low hit events since the time window is more likely to fall below the noise threshold too early.

5. Merge two clusters if t_{end} of the first cluster is within 30 ns of t_{start} of the second cluster.

Figure 14 shows the raw hit-time distribution for a neutrino interaction event. A special noise-off MC was generated with the same event seeds[2] to evaluate the performance of the algorithm for finding true hits amongst noise. The hits from the noise-off MC are shown in colored histograms (different colors corresponds to different clusters), while the noise-on histogram is in gray. The true particles above Cerenkov threshold in the event are listed in the figure and their time of birth is plotted as colored vertical lines. The primary sub-event (green histogram) consists of a muon and a pion, which both decay to produce two subsequent sub-events (blue and yellow histograms). spliTChan applied to the noise-on MC properly builds a time cluster window around each set of hits and the resulting window contains all the "true" hits from the noise-off MC.

Figure 15 is another, more complicated, example showing the case where two clusters are merged. The first cluster (green histogram) contains true particles at two times, 965 ns and 1412 ns, producing two visible peaks in the timing distribution. The two peaks are close enough in time that spliTChan merges them into a single cluster. The peak finder (and Muechk in this case), however, is able to resolve such peaks, or sub-events, due to the TOF correction. These peaks that are contained in a single cluster are referred to as "in-gate" sub-events.

The amount of time extension, t_{extend} was determined using 1000 ν_{μ} (from T2K flux) events. We define the following variables to test the performance of the algorithm:

- *# of Hits in Cluster* ($nHits$): The total number of hits in the resulting spliTChan cluster with noise-on.

- *True hit*: A hit from the noise-off MC. *True hits* within a spliTChan cluster are associated with that cluster.

---

[2] A modified SKDETSIM was necessary to have consistent event seeding between the noise-on and noise-off mode. Ideally, the MC should provide truth information for each hit, however this was currently computationally unfeasible.
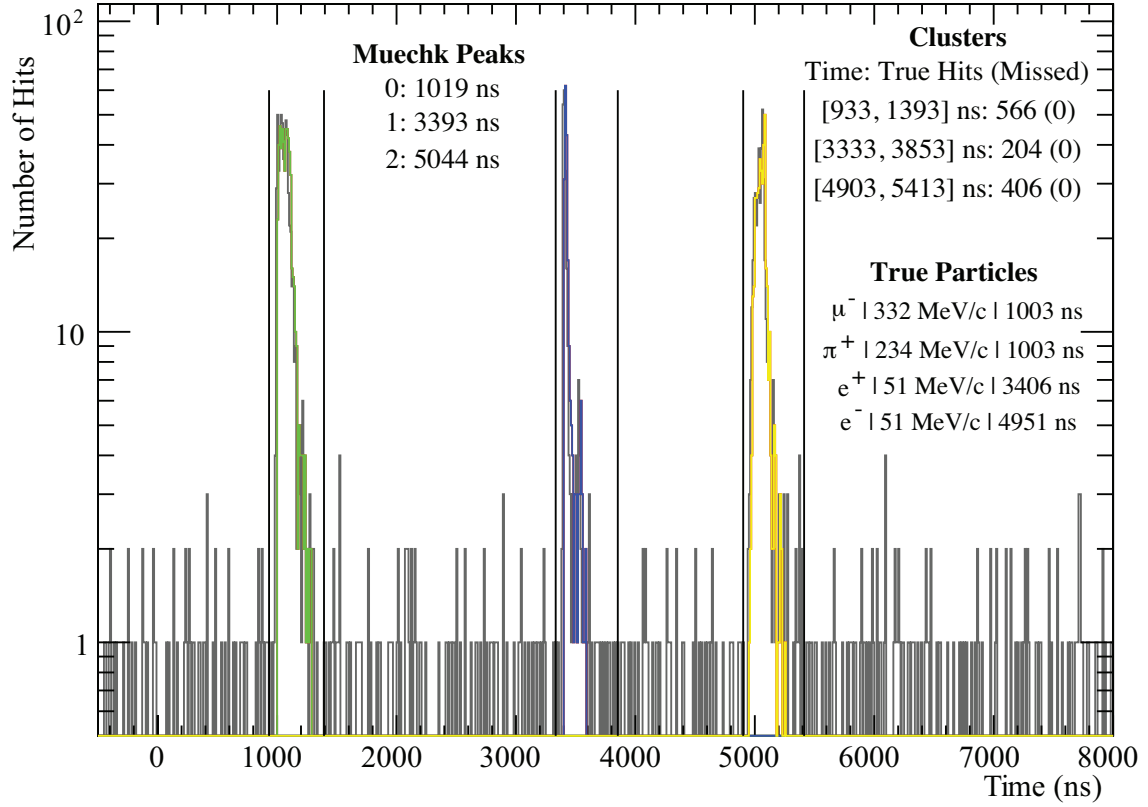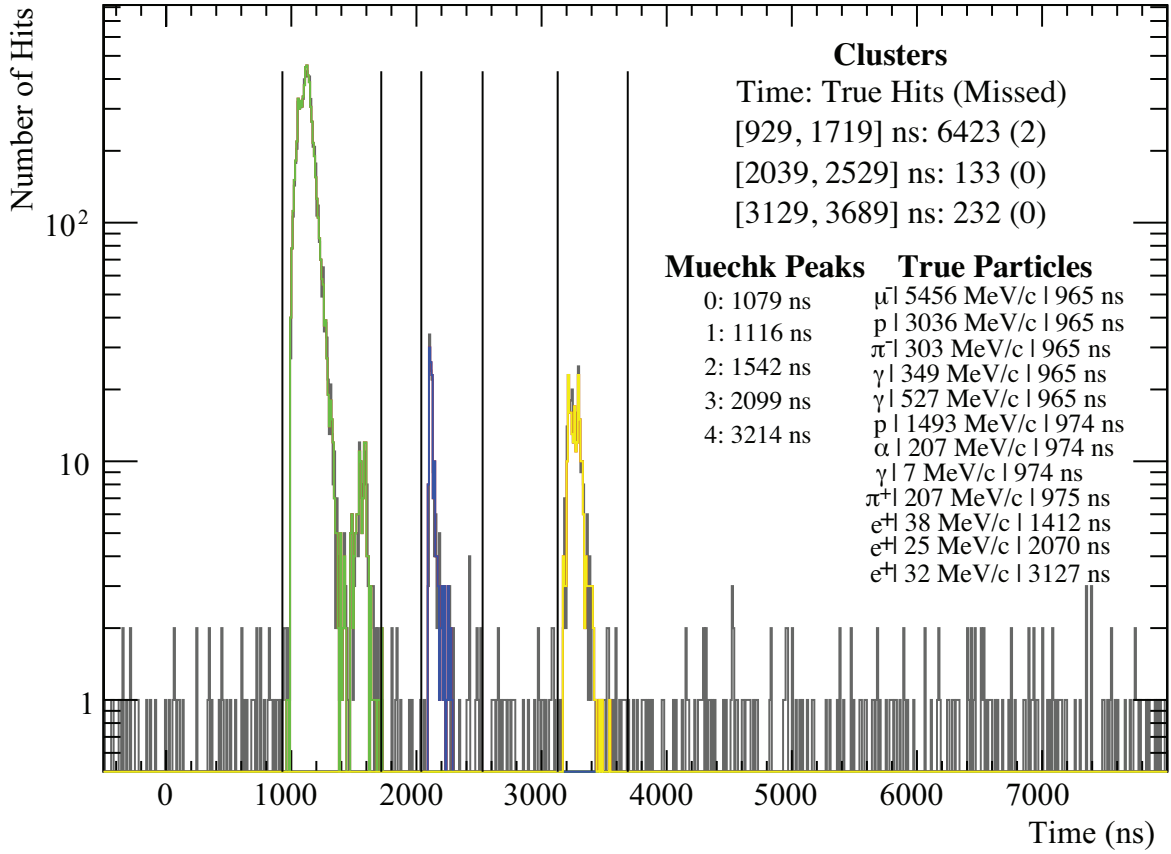
Figure 14: Number of hits as a function of raw time for a neutrino interaction event. The gray histogram is noise-on MC, while the colored histograms are noise-off. The black vertical lines correspond to the start (t_{start}) and end (t_{end}) times of the spliTChan clusters listed in the figure. The Muechk peak (TOF corrected) times are also listed. True particles above Cherenkov threshold and their birth-times are listed, and show good correspondence with the identified clusters.

- *Missed true hit*: A *true hit* that does not lie in a spliTChan cluster applied to the noise-off MC. It is associated to a cluster if it lies within 9/10 of the time to the next cluster (if any), since hit-time tails are expected to be long while rise-times are short. If there is no subsequent cluster, then it is associated to the nearest cluster unless it occurs closer to a true particle (*missed cluster*, below).

- *Fraction of missed true hits*: Number of *missed true hits* divided by the total number of *true hits* (including *missed true hits*) associated to a cluster.

- *Max(Δt from cluster end)*: The time difference between the latest *missed true hit* and t_{end} of the associated cluster.

- *Missed cluster*: A set of *true hits* that are not contained in a spliTChan cluster and occur closer in time to a true particle than to the edge of any cluster.

21

Figure 15: Number of hits as a function of raw time for a neutrino interaction event. The gray histogram is noise-on MC, while the colored histograms are noise-off. The black vertical lines correspond to the start (t_{start}) and end (t_{end}) times of the spliTChan clusters listed in the figure. The Muechk peak (TOF corrected) times are also listed. True particles above Cherenkov threshold and their birth-times are listed, and show good correspondence with the identified clusters.

Figure 16 shows the distributions for these variables with no time extension. The bottom-right panel shows the number of events for a given *fraction of missed true hits*. There is a significant number of events that miss up to 10% of *true hits* in a cluster. This is shown as a function of the *# of hits in the cluster* in the top right panel. Here it can be seen that the *fraction of missed true hits* increases as the total *# of hits in the cluster* decreases as expected. Then in the top-left panel, the *max(Δt from cluster end)* is shown as a function of *# of hits in the cluster*, where the histogram is filled by events weighted by the *fraction of missed true hits*. This gives an idea of the region with the most significant loss of *true hits* (mostly at low *# of hits in the cluster*). A line is drawn to give the time extension (t_{extend}) necessary to catch most of the *missed true hits*: $max(\Delta t \text{ from Cluster End}) = -\frac{320}{800} \times nHits + 320$.

    With this time extension applied, the *fraction of missed true hits* for most events becomes < 1% in Figure 17.

    The bottom left panel shows the distribution of # of *true hits* in a *missed cluster*, which is
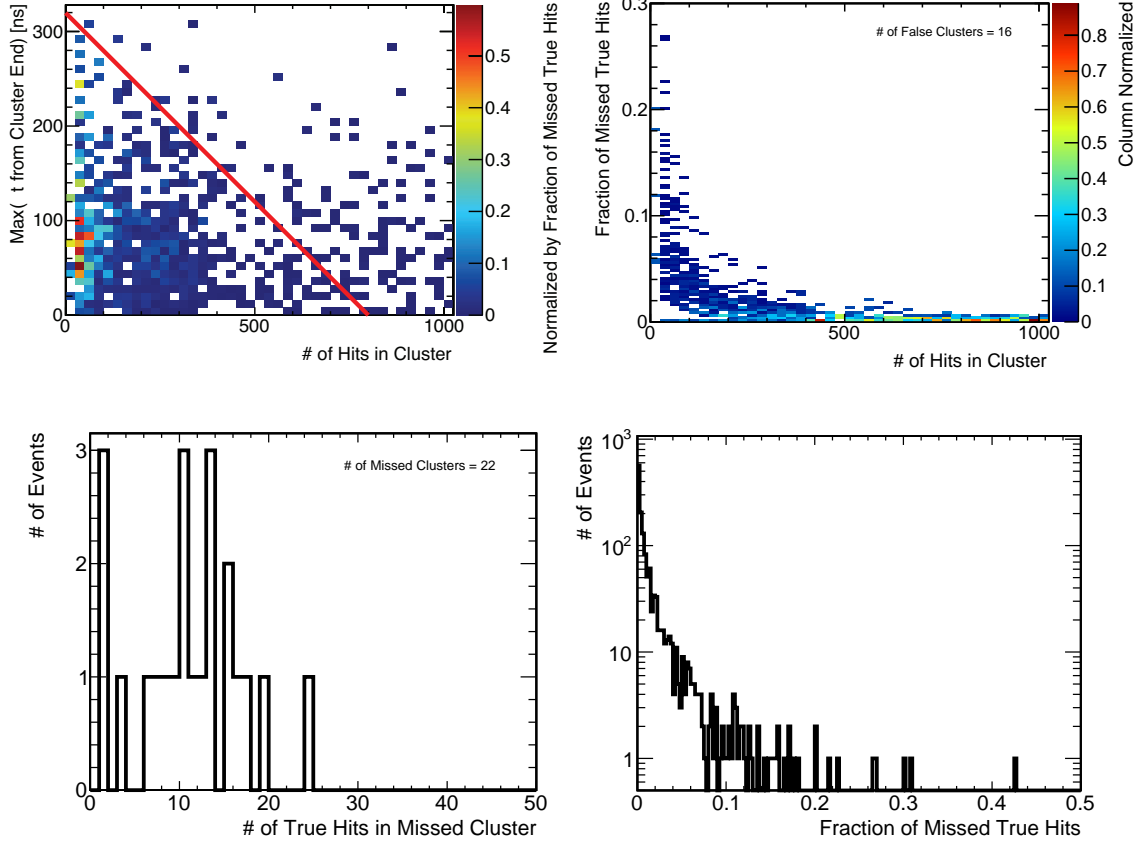
22

Figure 16: Distributions for the variables defined in the text for 1000 ν_μ events. No time extension is applied in the spliTChan algorithm.

simply too low (below noise threshold) for spliTChan to detect and does not change much when applying the time extension.

4.3 In-Gate Subevents

After time clusters are defined by spliTChan, each subevent that was found by the peak finder is associated with one of the clusters. This is simply done by evaluating the vertex goodness Eq.(21) at the time of the subevent peak in each of the time clusters. If a cluster contains hits that are associated with the subevent, the goodness takes a large value; for any other clusters the goodness becomes ≈ 0 since magnitude of the residual time Eq.(22) becomes too large for hits in such clusters. We therefore associate a subevent to a cluster in which the goodness is greater than η, which was discussed in Section 4.1. A subevent peak is discarded if it was not associated with any cluster. Similarly, a cluster not containing any subevent is determined as a fake cluster, and is therefore ignored.

Henceforth, let us refer to the clusters that do contain subevents as "time windows". As it will be apparent from later discussions, the full likelihood fitting by fiTQun is done at least once in each of the time windows, and during a fit, only the hits that are contained in the concerned time window are used. We can therefore fit subevents that are contained in different
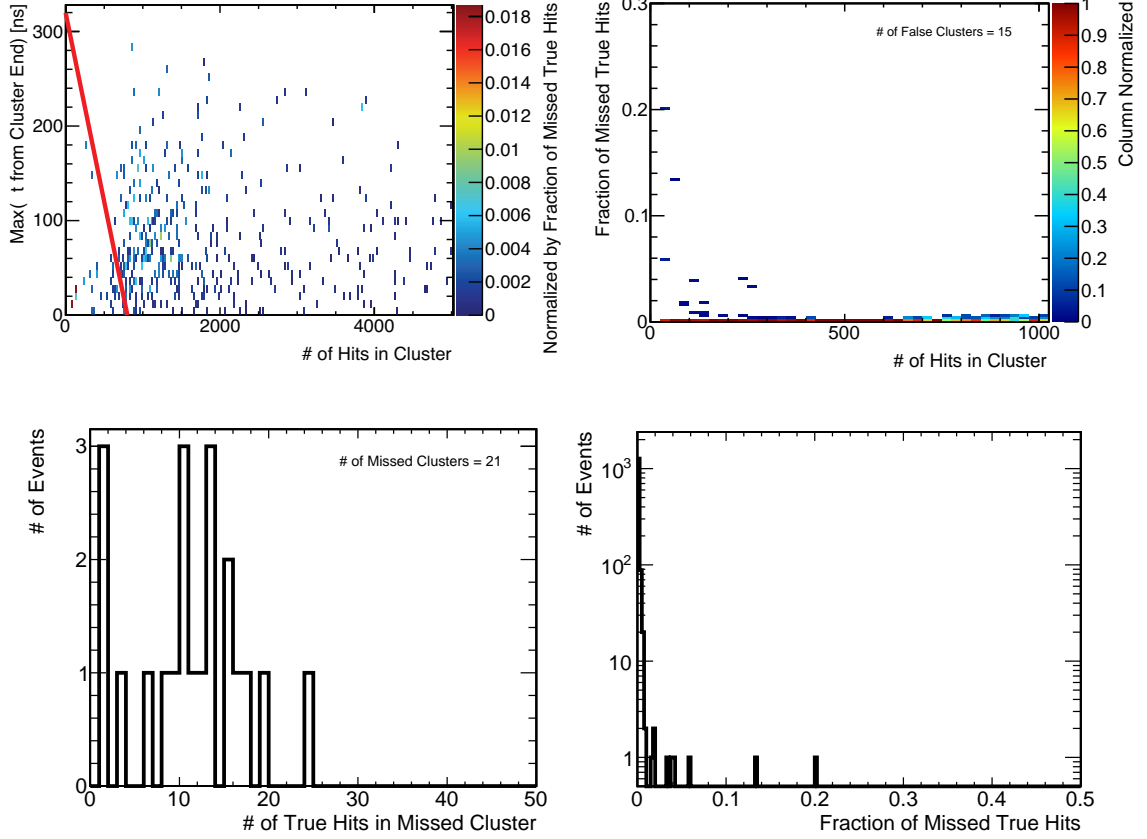
23

Figure 17: Distributions for the variables defined in the text for 1000 ν_μ events. The time extension is applied in the spliTChan algorithm.

time windows independently of each other.

After the peak and cluster association, we have subevent information for each of the time windows, and some windows contain multiple subevents. We refer to such multiple subevents in a time window as "in-gate" subevents. When reconstructing a subevent, only the hits that are contained in its associated time window are used as it was mentioned above, and thus in case there is only one subevent in the window, the fitter uses all the hits in the window. However, when there are in-gate subevents, we need to allocate the hits among multiple subevents.

The allocation procedure starts by associating the hits in the time window to subevents other than the first subevent in the time window; for brevity, let us refer to such subevents as "secondary in-gate subevents". A hit is associated with a secondary in-gate subevent when

$$-30\text{ns} < T_{\text{res}}^i < 60\text{ns}, \tag{25}$$

where T_{res}^i is the residual time defined in Eq.(22), calculated with the pre-fit vertex and the subevent peak time. Thus, when reconstructing a secondary in-gate subevent, all hits that satisfy the condition Eq.(25) are used when evaluating the likelihood function, while all the other hit PMTs in the time window are ignored. Finally, the remaining hits in the time window that are not associated with any of the secondary in-gate subevents are allocated to the first subevent in the time window.

24

In order to see how the procedures described above work, event displays of an MC event which has an in-gate decay electron are shown in Figure 18. As it is clear from the hit time distribution on the right, in addition to the rings of the primary particles, there is a ring from an in-gate decay electron in the upper half of the figures, which was observed considerably later compared to the other rings. The peak finder finds two in-gate subevents in this event, and after the hit allocation among the subevents is done, the charge distribution for hits that are associated with each of the two subevents is separately shown in Figure 19. As it can be seen from the figures, rings from the primary particles and the in-gate decay electron are clearly separated.
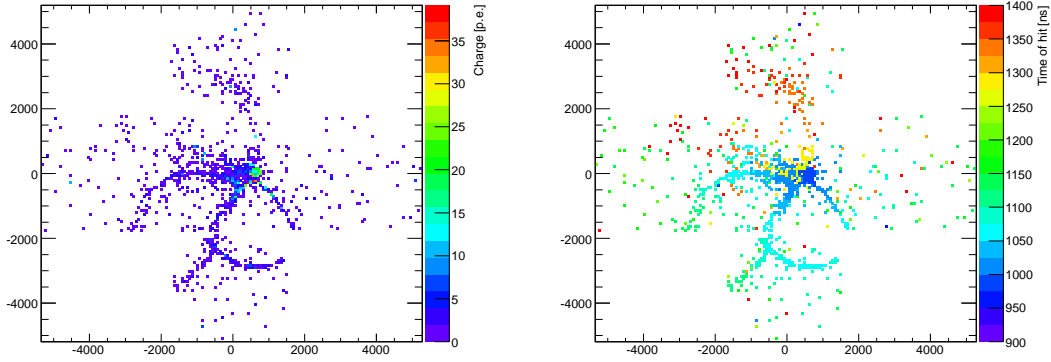
Figure 18: Event displays of an MC event which has an in-gate decay electron. The left plot shows the distribution of the charge of each hit in the time window, and the right plot shows the hit time. In addition to the rings due to the primary particles, a ring from an in-gate decay electron is visible in the upper half of the figures, and they are clearly separated in time as it is seen in the right figure.
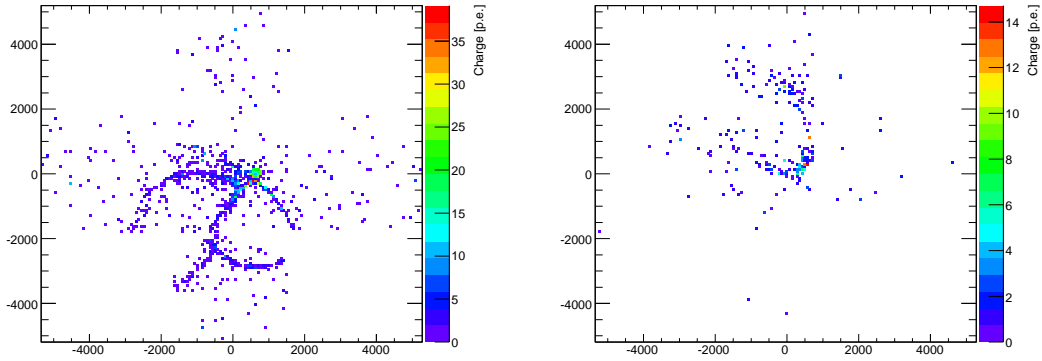

Figure 19: Charge distribution for hits that are associated with each in-gate subevent, for the same event which was shown in Figure 18. The left figure shows the hits allocated to the first subevent, and the right is for the in-gate second subevent. As it can be seen from the figures, rings from the primary particles and the in-gate decay electron are clearly separated.

25

5   The Single-Ring Fitter

After the vertex pre-fitter and the subevent algorithms, the single-ring fitter is run on each subevent which was found by the peak finder. After initializing the particle track parameters to appropriate seeding values, the fitter preforms MINUIT minimization of the negative log of the single-ring likelihood function, which was constructed in Section 2. Fit procedures for the single-ring electron and muon hypotheses are described below.

The single-ring electron fit starts by setting the vertex position to the pre-fit values, and the time to the peak time. In order to determine the initial value for the direction, a likelihood scan of the direction is performed by sampling the likelihood at 400 points that are equally spaced on the unit sphere. For the direction scan, momentum is fixed at the value which is roughly estimated using the total observed charge. After the direction is determined by the grid scan, the final momentum seed value is set by performing another likelihood scan, this time, by only varying the momentum. Once all the seven track parameters are seeded, the parameters are then simultaneously fit by MINUIT minimization of the $-\ln L$ using the SIMPLEX algorithm, which provides the final best fit estimation of the track parameters.

Following the single-ring electron fit is the single-ring muon fit, which takes the vertex, time and direction from the electron fit result as their seed values. The momentum is then estimated by a likelihood scan, as it was done in the electron fit, after which the full simultaneous minimization of the $-\ln L$ is performed.

5.1   Performance

In this section, the performance of the single-ring fitter is tested on MC samples of electron and muon particle gun, as well as atmospheric neutrinos. In all the figures, the red histograms are fiTQun performance, while the overlaid black histograms are the corresponding APfit single-ring fit results.

5.1.1   Particle Gun Sample

Below are the performance plots on electron and muon particle gun MC samples, in which events are generated at random vertex and direction with momentum uniformly distributed below 1GeV/c. Fully-Contained, true fiducial, single-ring(by APfit) cuts are applied to the sample, and we also allow the presence of a decay electron in an event only if the decay happens more than 500ns after the software trigger based on MC truth information; if a decay happens earlier, the event is cut. This is to remove the influence of early decay electrons on the primary muon reconstruction, so that we can more purely evaluate the the single-ring fitters' performance on the primary muons. By this cut, we also remove events in which a decay electron was triggered and reconstructed as the primary particle instead of the muon, which inevitably happen when the primary muons are near or below the Cherenkov threshold. In all the figures, the left columns show the single-ring electron fit results on single electron events, and the right columns show the muon fit results on single muon events.

Figure 20 shows the distribution of the distance between the reconstructed and the true vertex position. The resolutions are defined as the 68.3 percentiles, which are indicated by the dashed arrows in the plots. The longitudinal distance as well as the transverse distance, with respect to the true particle direction, between the true and the reconstructed vertices are separately shown in Figure 21.
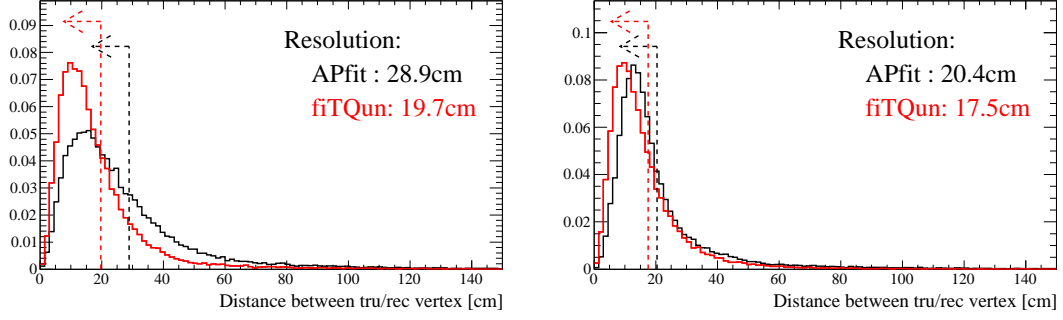
26

Figure 20: Distributions of the distance between the reconstructed and the true vertices, for single-ring electron(left) and muon(right) particle gun events. The red histograms are the distributions for fiTQun, and the black histograms are for APfit. The resolutions are defined as the 68.3 percentiles, which are indicated by the dashed arrows.
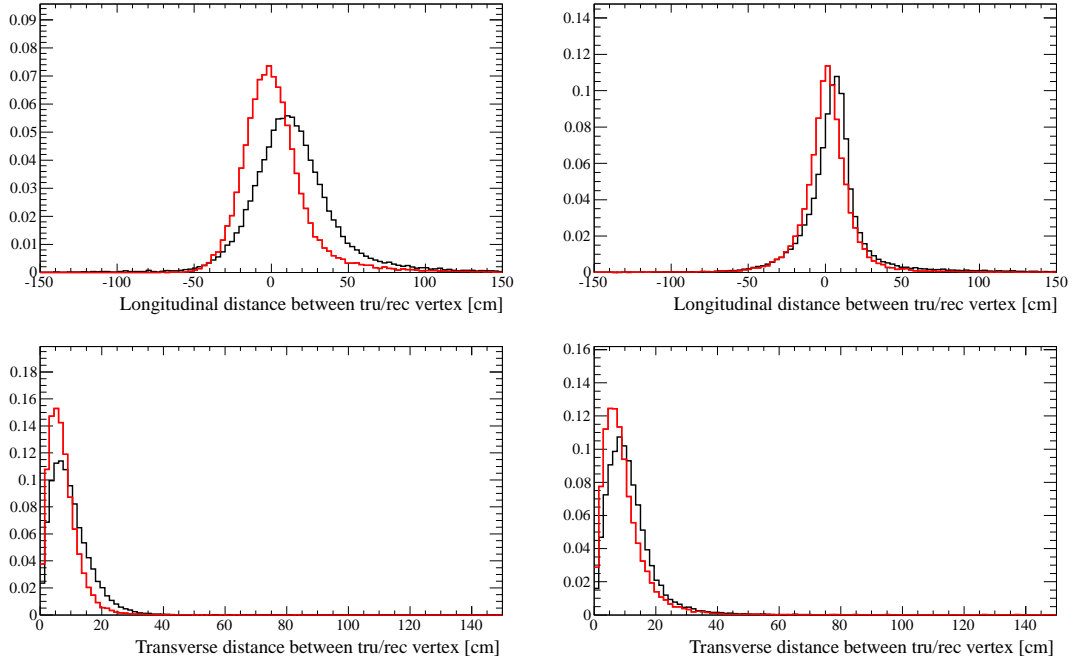

Figure 21: Distributions of the longitudinal(top) and the transverse(bottom) distance between the reconstructed and the true vertices, with respect to the true particle direction, for single-ring electron(left) and muon(right) particle gun events. The red histograms are the distributions for fiTQun, and the black histograms are for APfit.

27

Figure 22 shows the distributions of the angle between the true and the reconstructed particle directions. The resolutions are defined as the 68.3 percentiles, which are indicated by the dashed arrows.
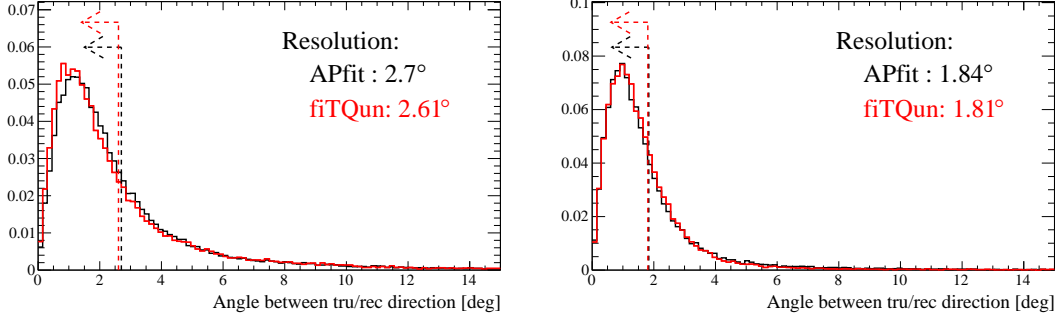

Figure 22: Distributions of the angle between the true and the reconstructed particle directions, for single-ring electron(left) and muon(right) particle gun events. The red histograms are the distributions for fiTQun, and the black histograms are for APfit. The resolutions are defined as the 68.3 percentiles, which are indicated by the dashed arrows.

Figure 23 shows the momentum resolutions and biases as functions of true particle momentum. The distribution of $(p^{\mathrm{rec}} - p^{\mathrm{tru}})/p^{\mathrm{tru}}$ is fitted by a Gaussian at each true momentum bin, and its peak position and the σ are reported as the bias and the resolution in the plots.

5.1.2 Atmospheric Neutrino Sample

Below are the performance plots on the atmospheric neutrino MC sample, with Fully-Contained, true fiducial, single-ring(by APfit) cuts applied. In all the figures below, the left columns show the single-ring electron fit results on ν_e CCQE events, and the right columns show the muon fit results on ν_μ CCQE events.

Figure 24 shows the distribution of the distance between the reconstructed and the true vertex position. The resolutions are defined as the 68.3 percentiles, which are indicated by the dashed arrows in the plots. The longitudinal distance as well as the transverse distance, with respect to the true outgoing lepton direction, between the true and the reconstructed vertices are separately shown in Figure 25.

Figure 26 shows the distributions of the angle between the true and the reconstructed directions of the outgoing leptons. The resolutions are defined as the 68.3 percentiles, which are indicated by the dashed arrows.

Figure 27 shows the momentum resolutions and biases as functions of true outgoing lepton momentum. The distribution of $(p^{\mathrm{rec}} - p^{\mathrm{tru}})/p^{\mathrm{tru}}$ is fitted by a Gaussian at each true momentum bin, and its peak position and the σ are reported as the bias and the resolution in the plots.

5.2 Particle Identification

In fiTQun, particle identification is done by comparing the best-fit likelihood values between different particle hypotheses. For example, electrons and muons are distinguished by making a cut on the log likelihood ratio $\ln(L_e/L_\mu)$ of the best-fit electron and muon hypotheses.
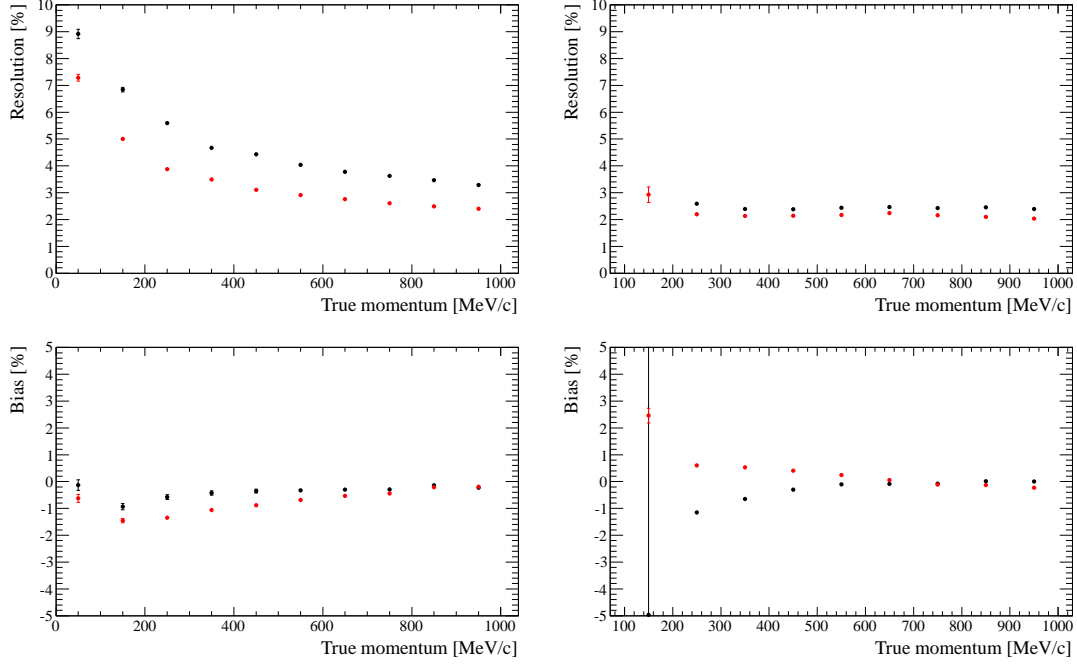
Figure 23: Momentum resolutions(top) and biases(bottom) for single-ring electron and muon(right) particle gun events, as a function of true momentum. The red markers indicate the performance of fiTQun, and the black markers are for APfit.
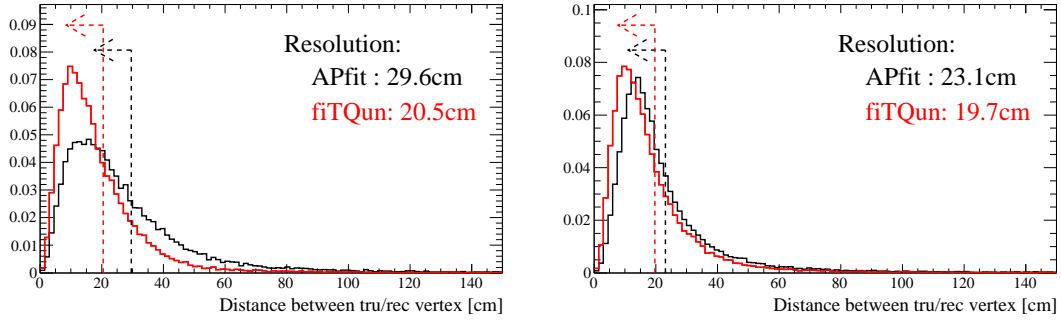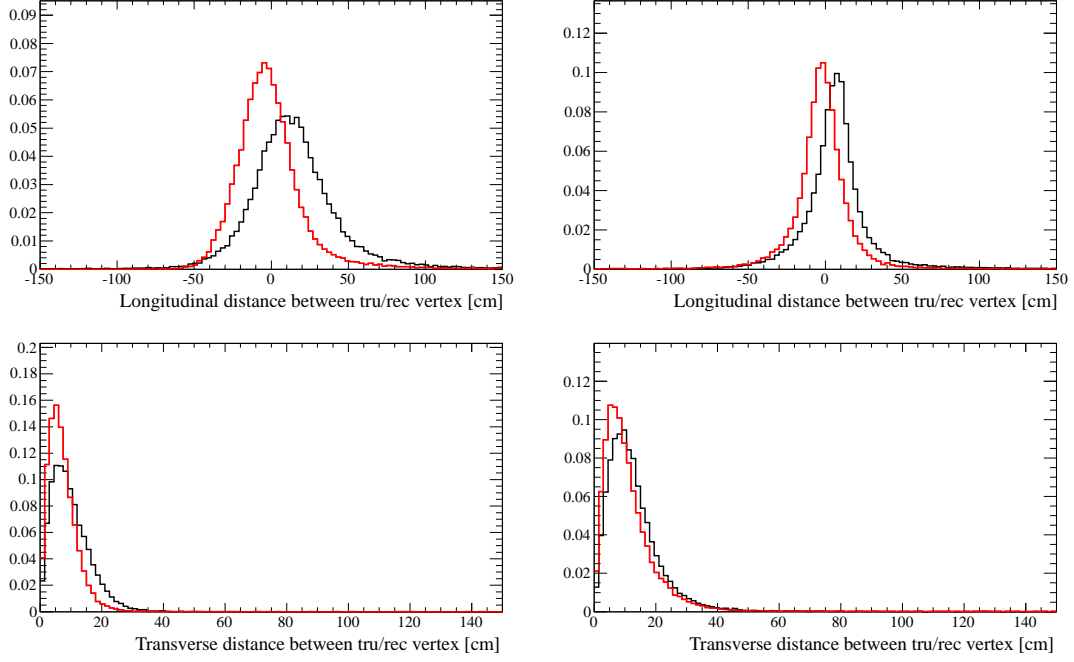

Figure 24: Distributions of the distance between the reconstructed and the true vertices, for single-ring atmospheric ν_e CCQE(left) and ν_μ CCQE(right) events. The red histograms are the distr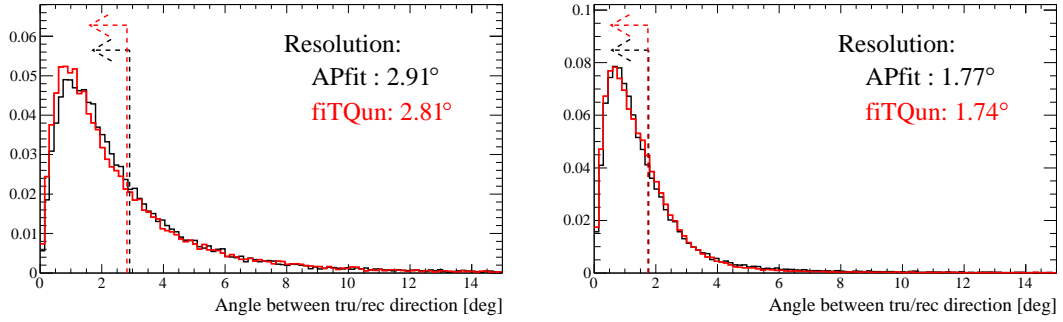ibutions for fiTQun, and the black histograms are for APfit. The resolutions are defined as the 68.3 percentiles, which are indicated by the dashed arrows.

Figure 25: Distributions of the longitudinal(top) and the transverse(bottom) distance between the reconstructed and the true vertices, with respect to the true outgoing lepton direction, for single-ring atmospheric ν_e CCQE(left) and ν_μ CCQE(right) events. The red histograms are the distributions for fiTQun, and the black histograms are for APfit.

Figure 26: Distributions of the angle between the true and the reconstructed directions of the outgoing leptons, for single-ring atmospheric ν_e CCQE(left) and ν_μ CCQE(right) events. The red histograms are the distributions for fiTQun, and the black histograms are for APfit. The resolutions are defined as the 68.3 percentiles, which are indicated by the dashed arrows.
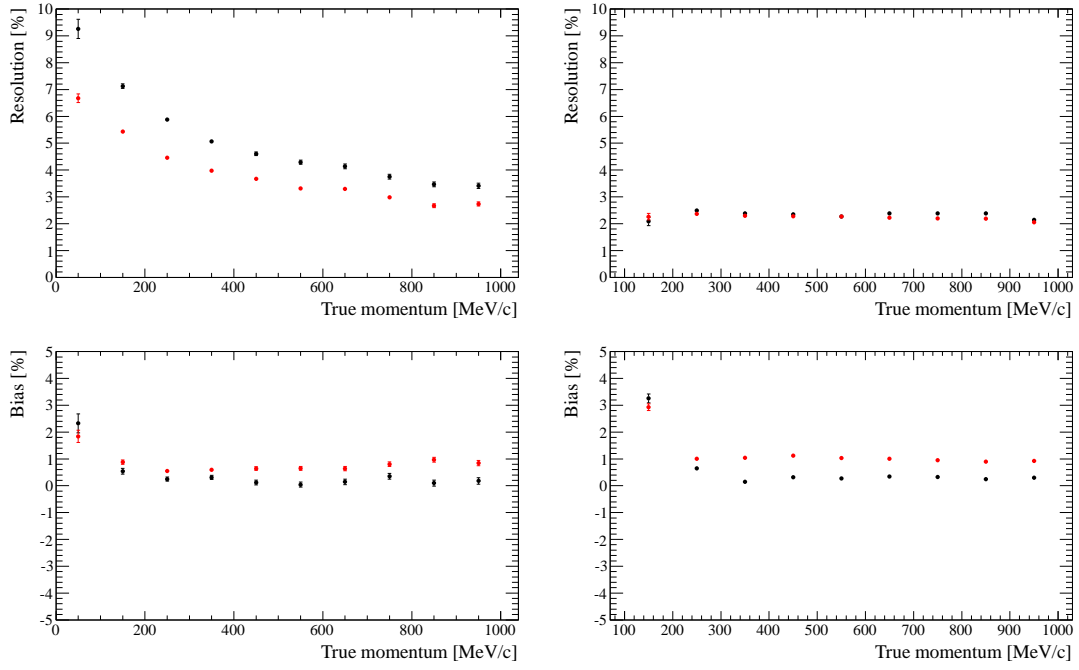
Figure 27: Momentum resolutions(top) and biases(bottom) for single-ring atmospheric ν_e CCQE(left) and ν_μ CCQE(right) events, as a function of true outgoing lepton momentum. The red markers indicate the performance of fiTQun, and the black markers are for APfit.

Figure 28 shows the likelihood separation of single-ring electron and muon particle gun events. The vertical axes are $\ln(L_e/L_\mu)$, and the horizontal axes are the reconstructed single-ring electron fit momentum. As it can be seen from the figure, electron events are clearly separated from muon events by making a line cut, which is defined as:

$$\ln(L_e/L_\mu) > 0.2 \times p_e^{\mathrm{rec}}[\mathrm{MeV/c}]. \tag{26}$$

The misidentification rate of electron and muon particle gun events are shown as a function of APfit visible energy in Figure 29. The early-decay cut, which was mentioned earlier, as well as Fully-Contained, true fiducial, single-ring selections, are applied to the sample.
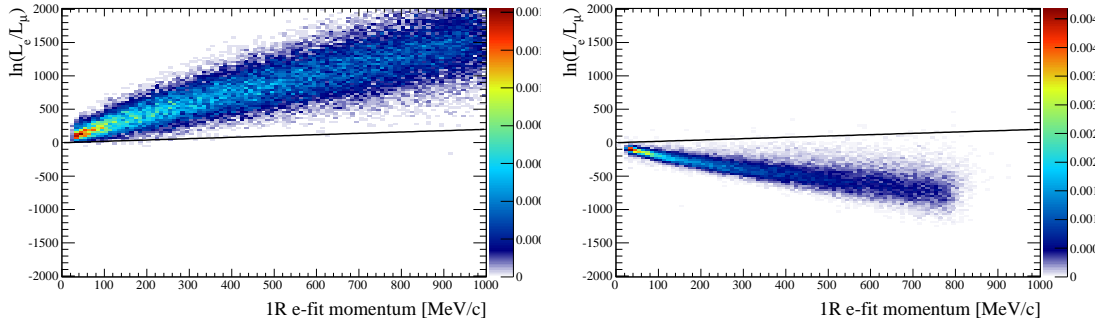

Figure 28: Likelihood separation of single-ring electron(left) and muon(right) particle gun events. The vertical axes are $\ln(L_e/L_\mu)$, and the horizontal axes are the reconstructed single-ring electron fit momentum. The black lines indicate the cut criteria for electron-muon separation.
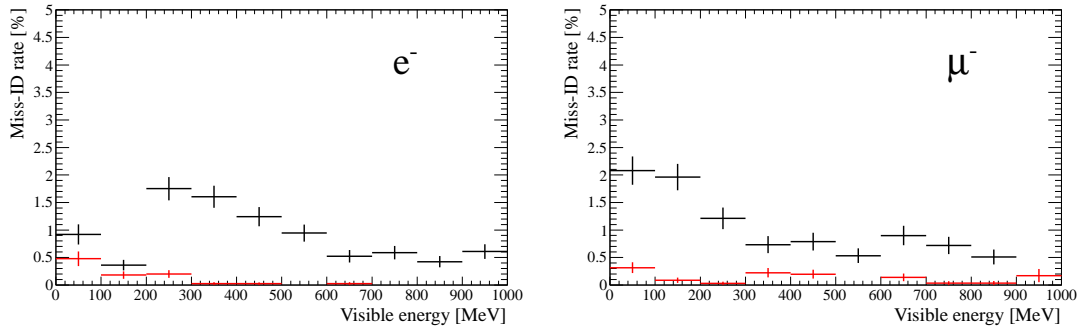

Figure 29: Misidentification rate of single-ring electron(left) and muon(right) particle gun events, binned by APfit visible energy. The red markers indicate the performance of fiTQun, and the black markers are for APfit.

Figure 30 shows the likelihood separation of single-ring atmospheric ν_e CCQE and ν_μ CCQE events. Since the early-decay cut is not applied here, there are low-energy events above the cut line in the right plot which are events in which the primary muon is near or below the Cherenkov threshold, and the decay electron was triggered and reconstructed instead of the muon. The misidentification rate of ν_e CCQE and ν_μ CCQE events are shown as a function of

32

⁵⁷⁸ APfit visible energy in Figure 31. In order to examine the PID performance of the single-ring
⁵⁷⁹ fitters, independent of the efficiency of the APfit ring counting, we require that no π^0's, π^+'s
⁵⁸⁰ and protons above Cherenkov threshold to be present in the final state, in addition to the Fully-
⁵⁸¹ Contained, true fiducial, single-ring criteria. Note that other visible particles such as nuclear
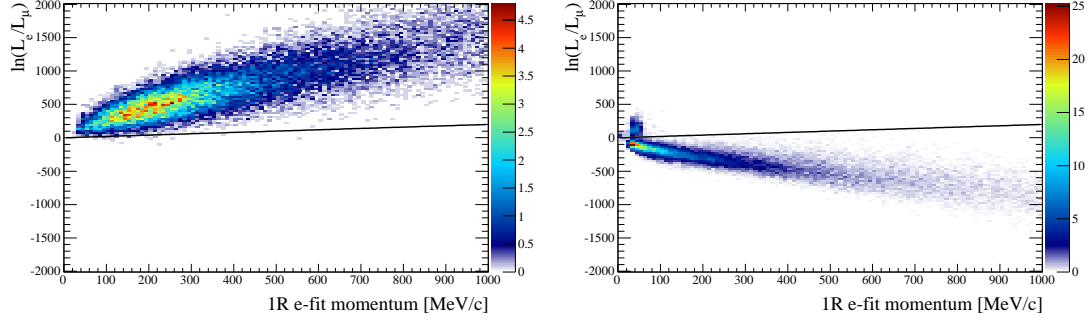de-excitation γ's are still present after the selections.

Figure 30: Likelihood separation of single-ring atmospheric ν_e CCQE(left) and ν_μ CCQE(right) events. The vertical axes are $\ln(L_e/L_\mu)$, and the horizontal axes are the reconstructed single-ring electron fit momentum. The black lines indicate the cut criteria for electron-muon separation.
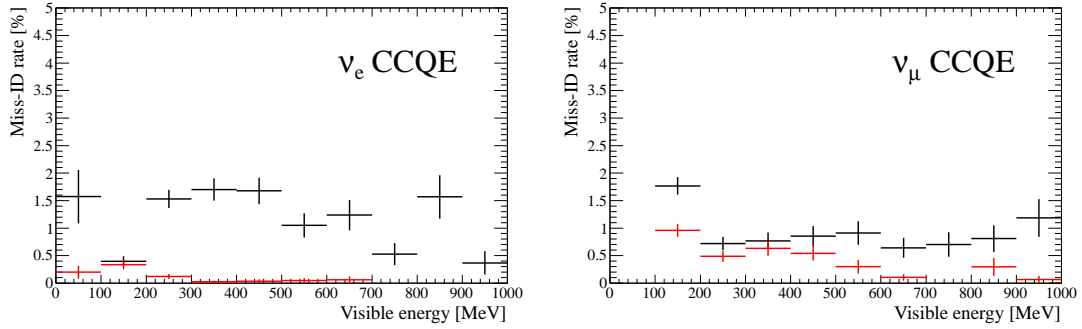

Figure 31: Misidentification rate of single-ring atmospheric ν_e CCQE(left) and ν_μ CCQE(right) events, binned by APfit visible energy. The red markers indicate the performance of fiTQun, and the black markers are for APfit.

⁵⁸²

33

6 Fitting Multiple Track Final States

The single-track formalism can be extended to fit hypotheses that involve multiple tracks. For each track in an event, a predicted charge and both scattered- and direct-light residual-time PDFs are calculated as described in Section 2. The predicted charge for each PMT is just the sum of the predicted charges from each of the individual tracks.

To determine the time likelihood for a multi-track event, Equations 18 and 19 must be extended. For a given PMT, each track is ordered according to the time-of-flight (i.e. distance) from the center of the track to the PMT. It is then assumed that the light from closer tracks will always reach the PMT before light from further tracks, and the direct light from all tracks will reach the PMT before scattered light from any of the tracks,

$$f_t(t^{res}) = \sum_{j=1}^{N_{tracks}} \left[w_j^{dir} f_t^{dir}(t^{res}) + w_j^{sct} f_t^{sct}(t^{res}) \right] \tag{27}$$

where

$$w_j^{dir} = \frac{\left(\prod_{k=1}^{j-1} e^{-\mu_k^{dir}} \right) \left(1 - e^{-\mu_j^{dir}} \right)}{\left(1 - \prod_{k=1}^{N_{tracks}} e^{-\mu_k^{dir}} \prod_{m=1}^{N_{tracks}} e^{-\mu_m^{sct}} \right)} \tag{28}$$

$$w_j^{sct} = \frac{\left(\prod_{k=1}^{j-1} e^{-\mu_k^{sct}} \right) \left(1 - e^{-\mu_j^{sct}} \right)}{\left(1 - \prod_{k=1}^{N_{tracks}} e^{-\mu_k^{dir}} \prod_{m=1}^{N_{tracks}} e^{-\mu_m^{sct}} \right)} \left(\prod_{k=1}^{N_{tracks}} e^{-\mu_k^{dir}} \right) \tag{29}$$

6.1 Fitting π^0 Particles

The π^0 fit hypothesis consists of two of the standard electron-hypothesis tracks constrained to point back to the same 4-vertex. Since the electron tracks are produced via photon conversions, the vertices are allowed to start some distance downstream of the π^0 vertex itself, and this distance is fit for on an event-by-event basis. An illustration of the π^0 fit hypothesis is shown in Figure 32. In total, 12 parameters are required to fully specify the π^0 fit hypothesis:

- the event 4-vertex: X, Y, Z, T

- the direction of each photon: θ_1, ϕ_1, θ_2, ϕ_2

- the magnitude of the 3-momentum of each photon: p_1, p_2

- the conversion distance for each photon: d_1^{conv}, d_2^{conv}

With the likelihood function defined, the main task is then to seed the fit; the likelihood surface is not smooth over large variations in the fit parameters, therefore it is important to start the fit as close to the likelihood maximum as possible. The π^0 fit seed uses the result of the single-track electron-hypothesis fit to identify the first electron track. To find the second track, the π^0 likelihood function is evaluated with 100 uniformly distributed [6] choices of the direction of the second track. During this direction scan, the momentum of the second track is arbitrarily set to 50 MeV, and the conversion lengths of both photons are set near the mean photon conversion length in water. Since the mean photon conversion length peaks near 60 cm at 50 MeV, and then gradually falls off toward the asymptotic value of 46.39 cm for multi-GeV
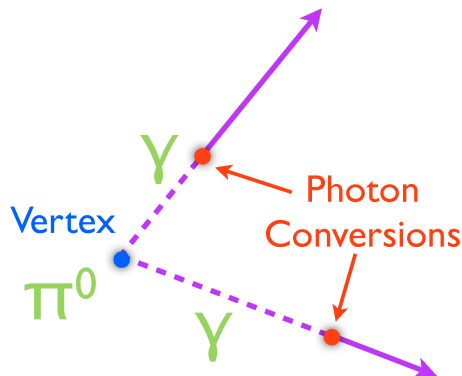
Figure 32: A cartoon of the components of the π^0 hypothesis fit is shown. Each photon has a direction, momentum, and conversion length, and both point back to a common vertex.

photons, a seed value of 50 cm was chosen. The direction that produces the lowest value of -ln(L) is chosen as the fit seed.

The second-track-direction scan produces an initial guess of all 12 π^0 fit parameters. However, the resulting seed momenta for the two photons are not well estimated. The single-track-electron fit tends to overestimate the momentum of first track due to the extra light produced by the other track in the event, and the momentum of the second ring was arbitrarily chosen. To improve the estimates of these parameters, a 2-parameter fit is performed in which only the momenta of the photons are allowed to vary while the other 10 parameters are fixed to the result from the direction scan. Once the seed is established a full 12-parameter π^0 fit is performed. The stages of the seeding for one example event are shown in Figure 33.

One additional modification to the π^0 fit seeding is needed to correct a particular failure mode of the single-track electron fit in events that contain 2 rings. If a low momentum π^0 decays about 4 m from an inner detector wall, it can produce a small ring on the closest wall, and large ring on the more distant, opposite wall. An example of such an event is shown in Figure 34. In this particular geometry, the single-track electron fit interprets the small ring as backward scattered light and pulls the vertex closer to the wall, as seen in Figure 35. To correct for this, any event in which the single-track fit has been pulled from the vertex prefit by more than 2.8 m is now shifted 4 m downstream before performing the second-track direction scan. The result of this modification can be seen in Figure 36. The bump in the π^0 mass spectrum around 10 MeV is removed with this change, and all of these events have migrated to the proper π^0 mass. The corresponding shoulder at low likelihood ratios has also been reduced.

All T2K event selections prior to the summer 2013 analysis used the POLFit reconstruction algorithm to find and reject π^0 events [3]. POLfit fixes the direction of the first photon ring to the result of the single ring, e-like fit, and only fits for the direction and energy fraction of the second ring (3 parameters). POLfit also does not use any PMT hit time information, and the scattering light prediction only comes from a Raleigh-like scattering model with no contribution from reflected light. More details an the POLFit algorithm can be found in T2K Technical Note 5 [3]. The remainder of this section will show the results of the fiTQun π^0 fit compared to those
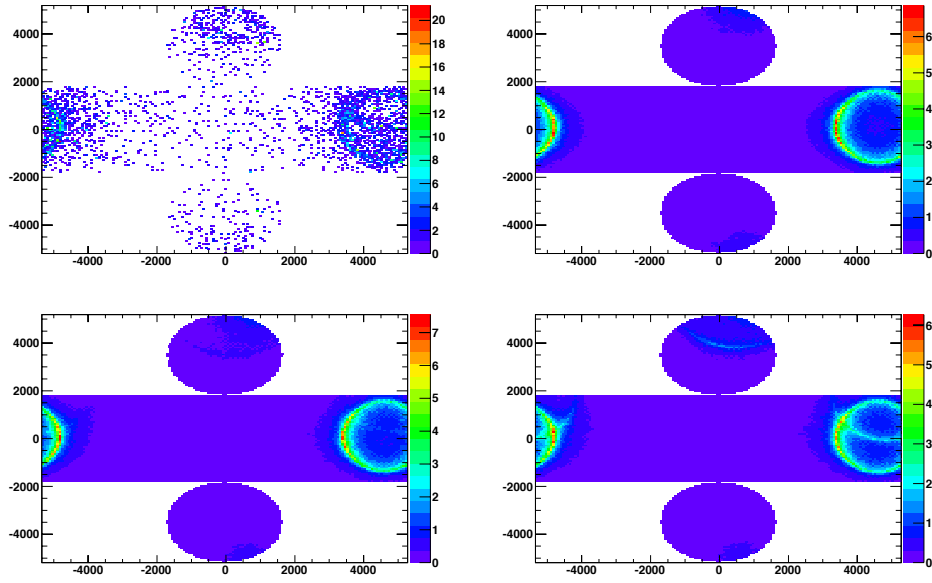
Figure 33: The stages of the π^0 fit are shown for one example event. The color z-axis shows the charge on each tube in photoelectrons. The top-left plot shows the measured charges for the event, the top-right plot shows the result of the single-track electron-hypothesis fit, the bottom-left plot shows the result of the direction scan for the second track, and the bottom-right plot shows the result of the full 12-parameter fit.
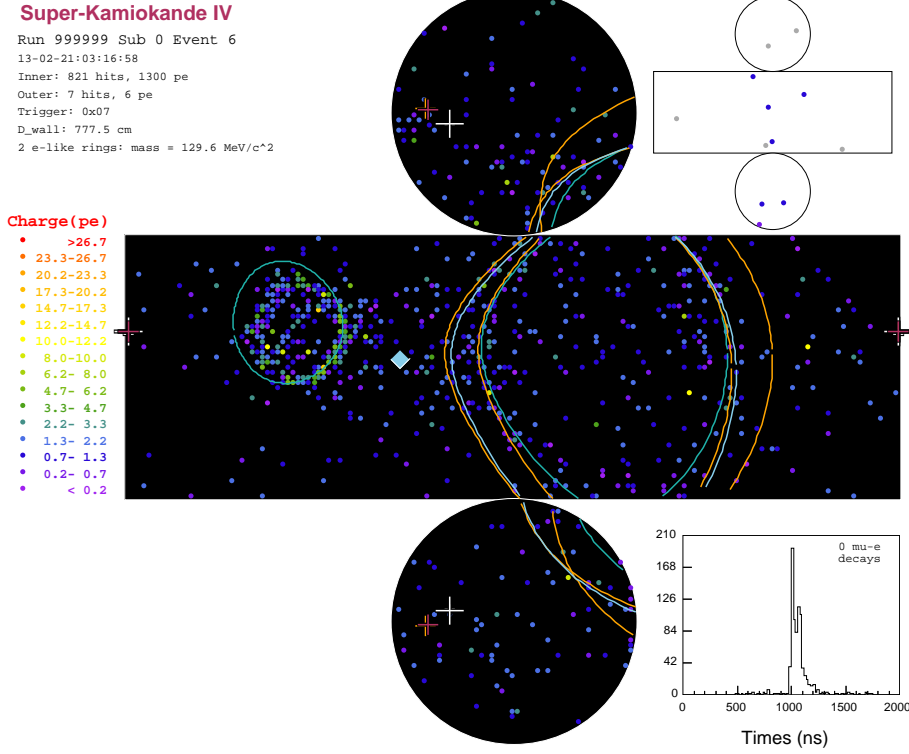
Figure 34: An example of an event with a true π^0 in which the single-ring electron fit vertex is shifted by several meters toward the upstream wall. The extra ring is interpreted by the fitter as back-scattered light.
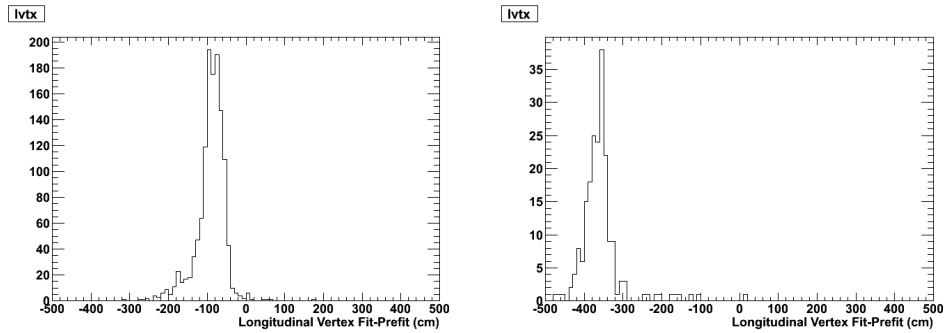

Figure 35: The shift in the reconstructed longitudinal vertex position between the vertex prefitter and the single-track electron hypothesis fit is shown for events that are properly reconstructed (left) and misreconstructed (right).

of POLFit.

Figure 37 shows the reconstructed π^0 mass for a π^0 particle gun with a flat momentum distribution between 0 and 500 MeV/c. The standard Super-K requirements of 1 e-like ring
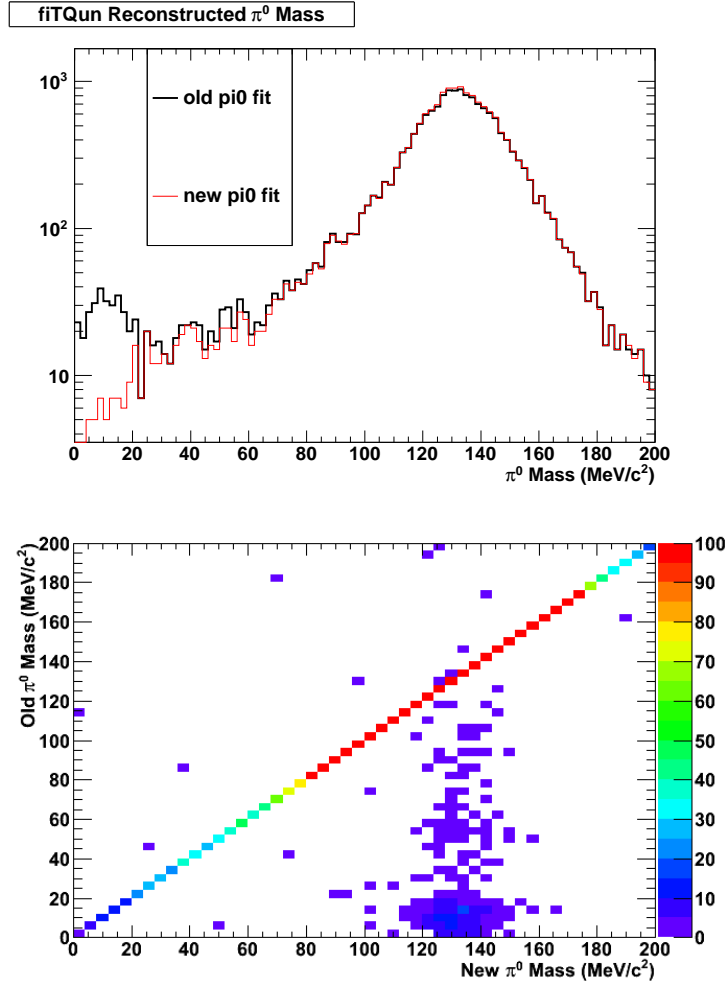
Figure 36: The π^0 particle gun results for the π^0 fit performance before (old) and after (new) the correction for the single-track electron vertex pull are shown. The new fit removes the tail in the π^0 mass distribution (top). The events that are removed from the tail now have the corrected reconstructed π^0 mass (bottom).

with more than 100 MeV of visible energy and that the events be within the fiducial volume have been applied. The fiTQun π^0 reconstruction shows no evidence for a spike at zero mass, and has a smoothly decreasing low-mass tail. The fraction of π^0 events surviving any given choice for a π^0 mass cut (and, hence, becoming background to a ν_e appearance measurement) is shown in Figure 38. In this sample, a cut below 80 MeV/c^2 would remove 70% of the background π^0 events that pass the POLFit cut. There is no significant difference in the APFit and fiTQun electron efficiency above π^0 masses of 60 MeV/c^2.

In previous T2K analyses, neutral pions were removed from the single-ring electron sample by selecting events with a reconstructed π^0 mass below 105 MeV/c^2. Using this cut value, the efficiency for rejecting a π^0 as a function of the lower energy of the two photons is shown in Figure 39. The additional power rejection power of fiTQun is largely due to improved detection of lower energy photons.
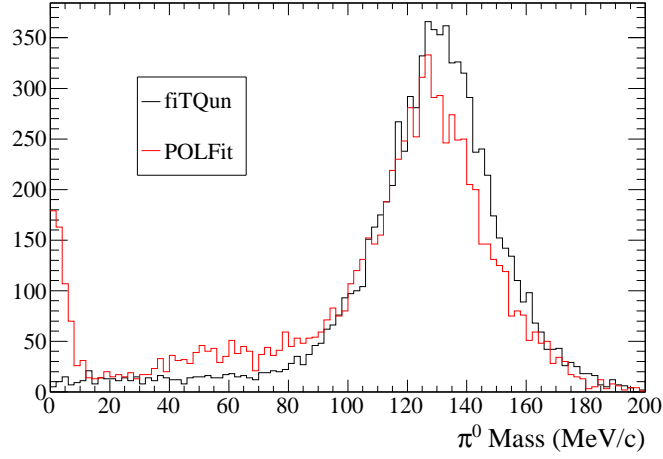
Figure 37: The π^0 mass distribution is shown for both POLFit and fiTQun using a π^0 particle gun sample with a uniform momentum distribution between 0 and 500 MeV/c. The 1-ring, e-like, $E_{visible} > 100$ MeV, and fiducial volume cuts have been applied.
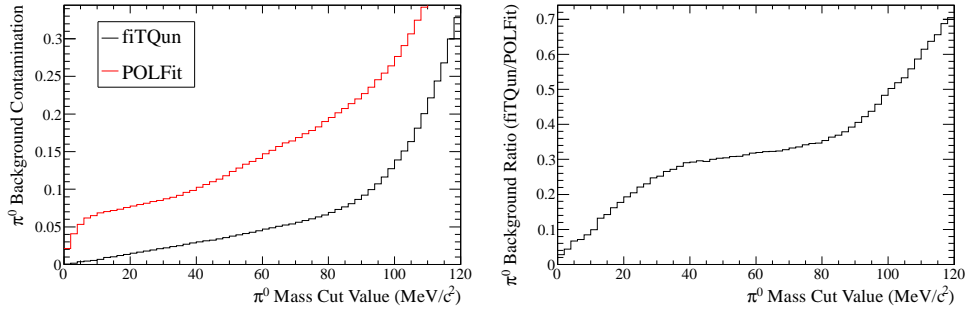

Figure 38: The left plot shows the fraction of π^0 that remain as a function of the choice of π^0 mass cut. The right plot shows the ratio of these fractions: fiTQun/POLFit. Below 80 MeV/c^2, fiTQun removes about 70% of the background retained by the POLFit mass cut.

Instead of using only the reconstructed π^0 fit mass to reject π^0 particles in a ν_e appearance seletion, it is possible to use both the mass and the likelihood ratio, which is most conveniently expressed in the form $ln(L_{\pi^0}/L_e)$. For the 2013 T2K ν_e appearance analysis, a 2-dimensional cut in likelihood vs π^0 mass space was used, as shown in Figure 40.

6.2   General Multi-Track Fitter

The current version of fiTQun contains a multi-ring fitter that runs 2-, 3-, and 4-ring fits assuming every combination of $e^\pm$ and μ/π rings. Since this fitter is not yet used in any official analysis, the details will be explained in a future update of this note.
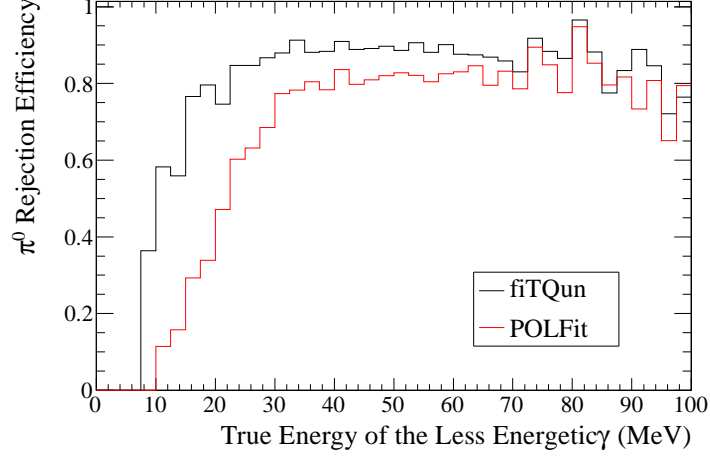
Figure 39: The efficiency for rejecting a π^0 with a π^0 mass < 105 MeV/c^2 is shown for both fiTQun and APFit as a function of the smaller of the two photon energies. The extra rejection power of fiTQun is largely due the improved ability to find lower energy photons.
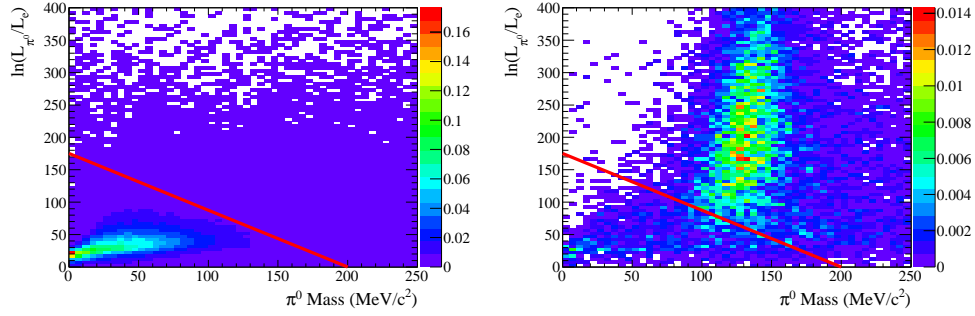

Figure 40: The log-likelihood ratio is shown for both ν_e-CC signal (left) and any background containing a π^0 (right) for T2K Monte Carlo events after all other ν_e selection cuts. The 2-dimensional line shows the cut used to remove the π^0 background in the ν_e appearance measurement.

7 Conclusion and Outlook

The fiTQun reconstruction algorithm provides a complete set of reconstruction tools for events at Super-K that is independent of all previously existing algorithms. The standard Super-K reconstruction tasks of subevent counting, ring counting, ring reconstruction, e/μ particle identification, and multi-ring fits can all be performed by fiTQun. In addition, fiTQun provides new functionality never before available in Super-K, such as $\pi^{\pm}$, $K^{\pm}$, and proton reconstruction, a mechanism by which all of these particle types can be distinguished, a custom π^0 fit to separate π^0's from electrons, and a new multi-ring fitter that incorporates particle identification information into the determination of the number and type of rings in an event. More details concerning these new features will be given in a future update of this note.

Performance advantages have already been seen in fiTQun over previously existing algorithms. The separation of electrons from neutral pions is significantly enhanced, the vertex and momentum resolution of the 1-ring fits improved, and the e/μ particle identification shows more discriminating power. Some of the new tools, such as the separation of charged pions from muons, have already given some indication that they may provide additional performance gains for both T2K and Super-K analyses.

With regard to processing power, fiTQun is similar to APFit for each type of fit that is performed, but the default configuration for fiTQun runs many more multi-parameter fits. If fiTQun is run in a configuration where only the 1-ring e-like, the 1-ring μ-like and π^0 fits are performed, which is all that is required from the ν_e appearance analysis, then it takes about 90% of the CPU time required for APFit. However, most of the CPU time in fiTQun is spent performing the 28 multi-ring fits that can be used to separate 1-ring, 2-ring, 3-ring, and 4-ring events. In the future, it should be possible to reduce the number of these fits by deciding which fits should be performed at runtime. This hasn't yet been done so that we can study to multi-ring fitter in more detail.

Testing the performance of the reconstruction on data is particularly important for fiTQun since it uses more information than previous algorithms and may be susceptible to previously undetected differences between the data and the Monte Carlo simulation. Detailed comparisons have been made between data and Monte Carlo performance using atmospheric neutrinos, stopping cosmic muons, and Michel electrons. The results of these studies are described in a separate note [2]. Additional comparisons between data and Monte Carlo events used to set the systematic uncertainties for the 2013 oscillation analysis were performed using hybrid-π^0 samples [4] and and a fit to Super-K atmospheric neutrino data [5].

At the time of this note, many of the new features of fiTQun have yet to be fully studied and exploited. Beyond the current suite of tools, the current machinery can be straightforwardly extended to produce custom fit hypotheses for any multi-particle final state. For example, the optimal way to reconstruct charged current, charged pion interactions is to write a dedicated $\mu + \pi$ fitter, the results of which can be compared to the various background hypotheses to optimally reconstruct the kinematics of these events separate them from the various background hypotheses. Many of the future improvements to fiTQun will be to implement such additional fit hypotheses.

References

[1] R. B. Patterson *et al.* "The extended-track reconstruction for MiniBooNE", Nuclear Instruments and Methods in Physics Research, **A608**, 206 (2009). arXiv:0902.2222 [hep-ex] (2009).

[2] S. Berkman *et al.* "Data/Monte Carlo Simulation Comparisons with fiTQun v3r1", T2K technical note, T2K-TN-153.

[3] S. Mine "New POLfit" T2K technical note, T2K-TN-005.

[4] T. Mueller and S. Mine "SK π^0 systematic errors for the ν_e analysis with T2K 6.4×10^{20} POT (Run 1-4) data", T2K technical note, T2K-TN-156.

[5] Y. Nishimura and H.-K. Tanaka "Super-K systematic uncertainties for the ν_e analysis with T2K 6.393×10^{20} POT (Run 1-4) data" T2K technical note, T2K-TN-157.

[6] E. B. Saff and A. B. J. Kuijlaars "Distributing Many Points on a Sphere", The Mathematical Intelligencer, **19**, 5 (1997).